Numerical investigations on unsteady vortical flows and transition over a cycloidal rotor at low Reynolds number

Lei Shi[1], Annie-Claude Bayeul-Lainé[1], Olivier Coutier-Delgosha[1,2, a)]

[1]Univ. Lille, CNRS, ONERA, Arts et Métiers ParisTech, Centrale Lille, UMR 9014 - LMFL - Laboratoire de Mécanique des Fluides de Lille - Kampé de Feriet, F-59000 Lille, France

[2]Kevin T. Crofton Department of Aerospace and Ocean Engineering, Virginia Tech, Blacksburg, VA 24060, USA

[a)]Author to whom correspondence should be addressed: Olivier.coutier-delgosha@ensam.eu

Abstract

The unsteady vortical flows and laminar-turbulence transition over a 2-bladed cycloidal rotor are investigated numerically at two advance coefficients, with special emphasis on the influence of two turbulence models, namely the original SST k-ω model and SST γ-$Re_{\theta t}$ transition model. The numerical results are compared with the existing numerical and experimental data, in terms of the global performance and detailed internal flow structures. The primary results show that increasing the advanced coefficient can't change the transition location of the performance for the single blade, but the magnitudes of these variables. Then, combined the forces acting on two blades and the blade loadings, the difference of the vertical force and propulsive force of the rotating system and single blade are clarified clearly for two turbulence models. Finally, at advancing side, the transition and its evolution on a single blade is elaborated. It shows that the SST γ-$Re_{\theta t}$ transition model is superior in predicting the overall performance, and is highly subjected to the disturbances, characterized by the large-scale vortex structures and massive flow separation, compared with SST k-ω model. Simultaneously, it has the capability to capture the transition process, from growing waves of the laminar boundary layer induced by the roll-up vortices to the fully generation of the separation bubble. It believes that this work can deep the understandings of underlying flow physics inside the cycloidal roto at low Reynolds number.

Keywords: Cycloidal rotor; SST γ-$Re_{\theta t}$ transition model; Vortical flows; Laminar-turbulence transition

1. Introduction

Cycloidal propeller, consisting of several vertical blades with the variable-pitch motion, has widely applications to many engineering equipment, involving the vertical-axis wind turbine (VAWT), underwater propulsion system and micro air vehicle (MAV). The main kinematic principle of a cycloidal propeller is that not only does the blade rotate around the shaft, but also it has a pitching motion around a pivot-point, as shown in figure 1. By changing the relative attack-of-angle θ_A (the angle between the blade chord and tangential direction of the blade rotating trajectory), the lift and propulsive force of the rotating system, induced by the sum of components of forces (lift and drag) acting on each blade, are produced continuously. Moreover, in a revolution, the blade would undergo the retreating and advanced sides, represented by the opposite blade geometry placement, which shows different vortex structures and the resultant blade loadings, because of the earlier flow separation near the sharp leading edge on the retreating side [1].

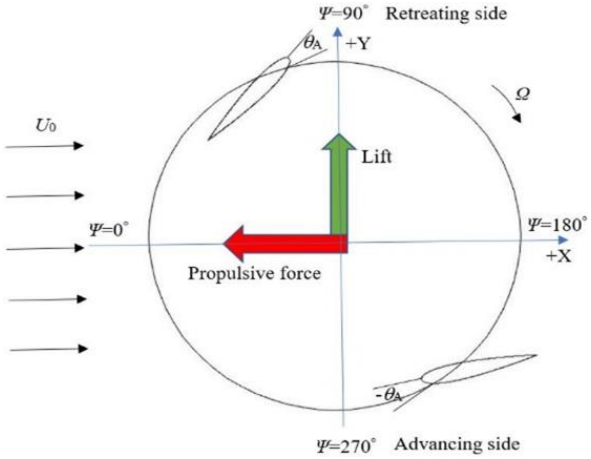

Fig.1 Sketch of a cycloidal rotor.

In a cycloidal rotor, there is a special event that should be paid more attention to: laminar-turbulence transition. At low Reynolds number, the airfoil/hydrofoil performance is adversely affected by the presence of a laminar separation bubble (LSB). Except for the increase of the drag, the LSB-induced undesirable effects, such as flow oscillation and abrupt stall, is always unavoidable. The formation of LSB is mainly caused by the separated laminar boundary layer which is subjected to the adverse pressure gradient. The shear layer is highly susceptible to disturbances, and transition to turbulence emerges through two-dimensional Kelvin-Helmholtz instability. Then, the energetic turbulent shear layer reattaches to the foil surface. However, the separation, transition and reattachment points depend on many parameters, including the incidence [2-3], Reynolds number [4-5], freestream turbulence level [6-7] and surface roughness [8]. For the moment, it proves that the conventional Reynolds-averaged Navier-Stokes (RANS) turbulence models only

resolve the fully turbulent flows without the consideration of the transition effect. Therefore, the RANS-based turbulence models coupled with the transition models are proposed, in which the Shear Stress Transport (SST) γ-$Re_{\theta t}$ transition model [9-10] achieves a good reputation and it has already been applied to many engineering flows. With application to the vertical-axis wind turbine, the SST γ-$Re_{\theta t}$ transition model shows the advantage in predicting the aerodynamic performance [11-13]. Additionally, Lam and Peng [14] clarified that the SST γ-$Re_{\theta t}$ has the same capability in capturing the time-averaged characteristics of VAWT wakes, compared with the Detached Eddy Simulation (DES). Furthermore, a lot of investigations concerning the influence of the pitch angle [15], existence of the shaft [16] and solidity [17], were conducted using the SST γ-$Re_{\theta t}$ model on VAWT. Recently, Lind et al. [18] employed the Spalart-Allmaras (SA) γ-$Re_{\theta t}$ model to study the internal flow structures of a cycloidal rotor at different advanced coefficients, and the primary results show that the aerodynamic performance and blade-wake interaction are predicted well. Based on the aforementioned investigations, it seems that the main focus is on the performance prediction and simple description of general flow structures. However, at low Reynolds number, the information about the transition on the blade due to the dynamic effect is not understood well.

The vortical flows inside the cycloidal propeller are extremely complicated, always involving the blade-wake and wake-wake interactions, the near-wall transitional flow and massive flow separation, which depends on the operating conditions and geometrical parameters remarkably. Until now, based on the experimental measurement and numerical simulation, some progress has been achieved in the prediction of the overall performance and flow structures over such devices. Paillard et al. [19] conducted the simulation on an active variable-pitch cross-flow Darrieus tidal turbine, with special emphasis on the sinusoidal pitch function. The results show that the function β=2(cos(2ωt)-1) results in the performance improvement by 52%. Then, Chen et al. [20] clarified that compared with the fixed-blade turbine, the turbine with the sinusoidal pitching blades has a much higher performance. With an appropriate pitching amplitude, the power efficiency increases and the fluctuation of the power output, rotating speed and torque output are suppressed obviously. Later on, Chen et al. [21] also proposed a novel sinusoidal pitching function, in which the blade has a fixed pitch in a limited range of the azimuthal angle, and the main results present that the power efficiency increases by 20%. For the 4-bladed cycloidal rotor, Benedict et al. [22] performed the experiments to check the influence of two important parameters, namely chord-to-radius ratio and pitch-pivot-point, on the global performance. The main conclusion is that the lift per unit power of the rotor is increases with the chord-to-radius ratio until the value of 0.67, while moving the pitch-pivot-point to the leading edge can

improve the lift-based efficiency. Then, Benedict et al. [23] analyzed the effects of different parameters on the cycloidal propeller performance comprehensively. It concludes that the optimal chord-to-radius is about 0.5-0.8 depending on the pitching amplitude, while increasing the solidity by increasing the blade chord can produce the higher power loading (thrust/power). Simultaneously, the asymmetrical pitching with a higher pitch angle at the top than at the bottom generates a better power loading, which is also reported by Benedict et al. [24-25]. Finally, the optimal pitch-pivot-point is almost located at 25-35% of the blade chord. In conclusion, it can be seen that the work on the cycloidal rotor is quite rare and most of them only concentrate on the performance prediction with various geometrical parameters and under different working conditions, but the detailed description of the internal flows and how the near-wall flow affects the performance of the rotating system and single blade is deserved to be investigated.

Inspired by the previous studies, the main purpose of the present work is to simulate the unsteady flows inside a two-bladed cycloidal rotor by SST γ-$Re_{\theta t}$ transition model, with special attention to the internal flow structures, involving the effect of the vortex evolution on the performance change and near-wall transitional flows, at two different advance coefficients. In addition, the results obtained by the transition model are compared with that of the original SST k-ω model. It believes that this work can shed light on the underlying flow physics of the cycloidal propeller under low Reynolds number condition and provide some experience to have a better design and optimization of such devices.

2. Turbulence modelling

2.1 SST k-ω turbulence model

The SST k-ω model is a two-equation eddy-viscosity model combining the Wilcox k-ω and k-ε models. The Wilcox k-ω model is well suitable for simulating flows in viscous sub-layer while the k-ε model is used to predict the flow behaviour far away from the wall. The choice of SST k-ω model as a baseline is for the reason that it accounts for the transport of turbulence shear stress and gives highly accurate predictions of the onset and the amount of flow separation under adverse pressure gradient [26]. The governing equations of SST k-ω are written as follows

$$\frac{\partial}{\partial t}(\rho k) + \frac{\partial}{\partial x_j}(\rho u_j k) = P_k - D_k + \frac{\partial}{\partial x_j}\left((\mu + \sigma_k \mu_t)\frac{\partial k}{\partial x_j}\right) \tag{1}$$

$$\frac{\partial}{\partial t}(\rho \omega) + \frac{\partial}{\partial x_j}(\rho u_j \omega) = \alpha \frac{P_k}{\nu_t} - D_\omega + Cd_\omega + \frac{\partial}{\partial x_j}\left((\mu + \sigma_\omega \mu_t)\frac{\partial \omega}{\partial x_j}\right) \tag{2}$$

The eddy viscosity μ_t used to close the equations, are given by

$$\mu_t = min\left[\frac{\rho k}{\omega}; \frac{a_1 \rho k}{SF_2}\right] \quad (3)$$

The information concerning the definitions of sources terms and values of parameters in these two equations can refer to the reference [26].

2.2 $\gamma - Re_{\theta t}$ transition model

The transport equations of intermittency γ and transition momentum thickness Reynolds number $Re_{\theta t}$ are given by

$$\frac{\partial}{\partial t}(\rho\gamma) + \frac{\partial}{\partial x_j}(\rho u_j \gamma) = P_\gamma - E_\gamma + \frac{\partial}{\partial x_j}\left(\left(\mu + \frac{\mu_t}{\sigma_f}\right)\frac{\partial \gamma}{\partial x_j}\right) \quad (4)$$

$$\frac{\partial}{\partial t}(\rho Re_{\theta t}) + \frac{\partial}{\partial x_j}(\rho u_j Re_{\theta t}) = P_{\theta t} + \frac{\partial}{\partial x_j}\left(\sigma_{\theta t}(\mu + \mu_t)\frac{\partial Re_{\theta t}}{\partial x_j}\right) \quad (5)$$

The definitions of the correlations and values of various parameters in these two equations are described minutely in reference [9-10].

2.3 Coupling $\gamma - Re_{\theta t}$ transition model with SST *k-ω* model

The effective intermittency γ_{eff} is used to bridge the $\gamma - Re_{\theta t}$ transition model with the original SST *k-ω* model by modifying the production and diffusion terms in turbulence kinetic energy equation, which is shown as follows

$$\frac{\partial}{\partial t}(\rho k) + \frac{\partial}{\partial x_j}(\rho u_j k) = \tilde{P}_k - \tilde{D}_k + \frac{\partial}{\partial x_j}\left((\mu + \sigma_k \mu_t)\frac{\partial k}{\partial x_j}\right) \quad (6)$$

$$\tilde{P}_k = \gamma_{eff} P_k;\ \tilde{D}_k = min\left(max\left(\gamma_{eff}, 0.1\right), 1.0\right) D_k \quad (7)$$

It can be seen that the SST γ-$Re_{\theta t}$ transition model is relatively simple, which has no direct relationship with the momentum equation and eddy viscosity of SST *k-ω* model, leading to the robustness improvement. Besides, it also shows the advantage in predicting the influence of high free-stream turbulence level on buffeted laminar boundary layer [9-10].

3. Problem descriptions

3.1 Geometry parameters and computational configuration

The two-dimensional 2-bladed cycloidal rotor is adopted in the present work and the main geometrical parameters are listed in Table 1. It should be noted that the blade operates with a sinusoidal motion and the pitching amplitude θ_{amp} is constant with a value of 35°. The initial position of the azimuthal angle ψ is from negative X axis, while the phase angle Φ changes from ψ=90° in anticlockwise direction. When the blades move in clockwise direction, bringing about the continuous generation of

the propulsive force in negative X axis and lift in positive Y axis, which is shown in figure 1. In this work, the flow structures are mainly studied at λ=0.52 and 0.73. The corresponding Reynolds numbers defined in Table 1 [27] are 3.56×10^4 and 3.91×10^4 respectively.

Table 1 Main geometrical parameters of the cycloidal rotor

Blade number (N_b)	2
Inlet velocity (U_0/(m/s))	5, 7
Blade chord (c/m)	0.0495
Blade profile	NACA0015
Rotor radius (R/m)	0.076
Rotating speed (n/(r/min))	1200
Pitching pivot location (%×c)	25
Blade pitching kinematics	$\theta_A=\theta_{amp}\sin(\psi+\Phi)$ (Φ=90°)
Advanced coefficient (λ)	$\lambda=U_0/\omega R$
Reynolds number (Re)	$Re=\sqrt{U_0^2+(\omega R)^2}c/\nu$

The rectangular computational domain is shown in figure 2a, which has an extension of 10c for the inlet section and 30c for the outlet region, based on the rotating center. The top and bottom walls have the same distance of 10c. In figure 2b, the sliding mesh technique is employed to control the propeller and blade movements by creating three periodic interfaces. The two small rotating circles covering the blades individually have the radius of c and they have the rotating and pitching motions simultaneously. The large rotating circle, which has a radius of 3c, only has the rotating motion.

The particle image velocimetry (PIV) measurements conducted in a closed-section wind tunnel were used to validate our simulations, in terms of the velocity and vorticity contours. The wind tunnel has a maximal velocity of 45m/s and the turbulence level is about 0.25%. The lift, propulsive force and shaft torque of the cycloidal rotor were measured by a precise 3-component wind tunnel force balance. The information of the experimental setup and the measurement precision accuracy is included in reference [28].

3.2 Mesh generation

The mesh distribution is critical to the laminar-turbulence transition, massive flow separation and unsteady wake. In the commercial code STARCCM +, the hybrid mesh, including the trimmed cell in the external region and prism layer cell near the blade surface, is employed in this work. To avoid existence vortex dissipation due to artificial diffusion in the rotor's wake, the densely meshed region around the rotor is extended up to the outlet boundary, as presented in figure 2a. Table 2 shows the mesh

distributions in two rotating parts covering two blades and near the blade surface at λ=0.52. The aspect ratio of 1.15 and prism layer thickness of 2×10^{-3} m are unchanged (shown in figure 2c) and the mesh arrangement near the wall depends on the number of the prism layer (from case 1 to case 4). In all tested cases, the target size has the same value with minimum size because of its weak effect. Case 2, 5 and 6 are used to check the influence of the streamwise mesh distribution by changing the target and minimum size near the blade surface while the effect of the mesh in two rotating parts (RP) are presented by case 2, 7 and 8. The time-averaged lift and propulsive force of the rotating system in last five rotations for different sets of meshes are compared with the available experiments [28]. It can be seen that there is a significant change of the lift and propulsive force when the prism layer increases to 70 and 75. In order to explain this particular event, the instantaneous vertical force coefficient C_{VF} ($C_{VF}=F_{VF}/(0.5*\rho*U_0^2*c)$, where F_{VF} is the vertical force) and propulsive force coefficient C_{PF} ($C_{PF}=F_{PF}/(0.5*\rho*U_0^2*c)$, where F_{PF} is the propulsive force) of one blade in the last rotation is plotted in figure 3. It seems that the discrepancy of the global performance obtained by different meshes becomes larger as the number of the prism layer increases. Therefore, an instant, at ψ=140° for right blade, is selected to study the detailed near-wall flow structures. The spanwise vorticity contours of different tested cases are presented in figure 4 and the results show that there are massive vorticity shedding on both sides of the blade. The distributions of vorticity for case 1 and 2 are almost the same, but it varies considerably for case 3 and 4, especially on the right surface. In figure 5, the velocity profiles on the right side at four locations are plotted and it shows that the results keep nearly same for case 1 and 2, but a little difference at the blade trailing edge where the flow separation occurs. However, the velocity profiles of case 3 and 4 are totally different, due to the vorticity shedding in figure 4. There are several reasons for that: (1) there is a little distortion of near-wall meshes in case 3 and 4; (2) this is presumably induced by the large value of specific turbulence frequency ω, which scales with the first grid point height [29]; (3) Very small y^+ ($y^+=yu_\tau/v$, where y is the distance to the wall, u_τ is the friction velocity and v is the kinematic viscosity) leads to the SST blending function switching to k-ε in the boundary layer, which is also observed in a compressor tested case [29]. Furthermore, by the comparison of meshes in case 2, 5 and 6, it can be seen that increasing the cells in the streamwise direction has a better performance. Then, the results of case 2, 7 and 8 show that further reduction of the mesh size in two rotating parts has a little deterioration of the performance, possibly due to the more resolved vortical flows. In conclusion, according to the above information, the mesh in case 7 is applied finally to all the following simulations.

Table 2 Mesh distributions and global performance prediction of tested cases

	Target size of the mesh in RP (m)	Minimum size of mesh in RP (m)	Target size of the mesh near the blade (m)	Minimum size of the mesh near the blade (m)	Number of the prism layer	Distance of the first layer to the wall (m)	Lift (N)	Propulsive force (N)
Case 1	7×10^{-7}	7×10^{-7}	2×10^{-7}	2×10^{-7}	60	6.8×10^{-8}	0.452	0.241
Case 2	7×10^{-7}	7×10^{-7}	2×10^{-7}	2×10^{-7}	65	3.4×10^{-8}	0.489	0.245
Case 3	7×10^{-7}	7×10^{-7}	2×10^{-7}	2×10^{-7}	70	1.7×10^{-8}	0.570	0.245
Case 4	7×10^{-7}	7×10^{-7}	2×10^{-7}	2×10^{-7}	75	8.4×10^{-9}	0.716	0.217
Case 5	7×10^{-7}	7×10^{-7}	8×10^{-7}	8×10^{-7}	65	3.4×10^{-8}	0.528	0.207
Case 6	7×10^{-7}	7×10^{-7}	5×10^{-7}	5×10^{-7}	65	3.4×10^{-8}	0.507	0.248
Case 7	6×10^{-7}	6×10^{-7}	2×10^{-7}	2×10^{-7}	65	3.4×10^{-8}	0.494	0.247
Case 8	5×10^{-7}	5×10^{-7}	2×10^{-7}	2×10^{-7}	65	3.4×10^{-8}	0.473	0.246
EXP							0.490	0.260

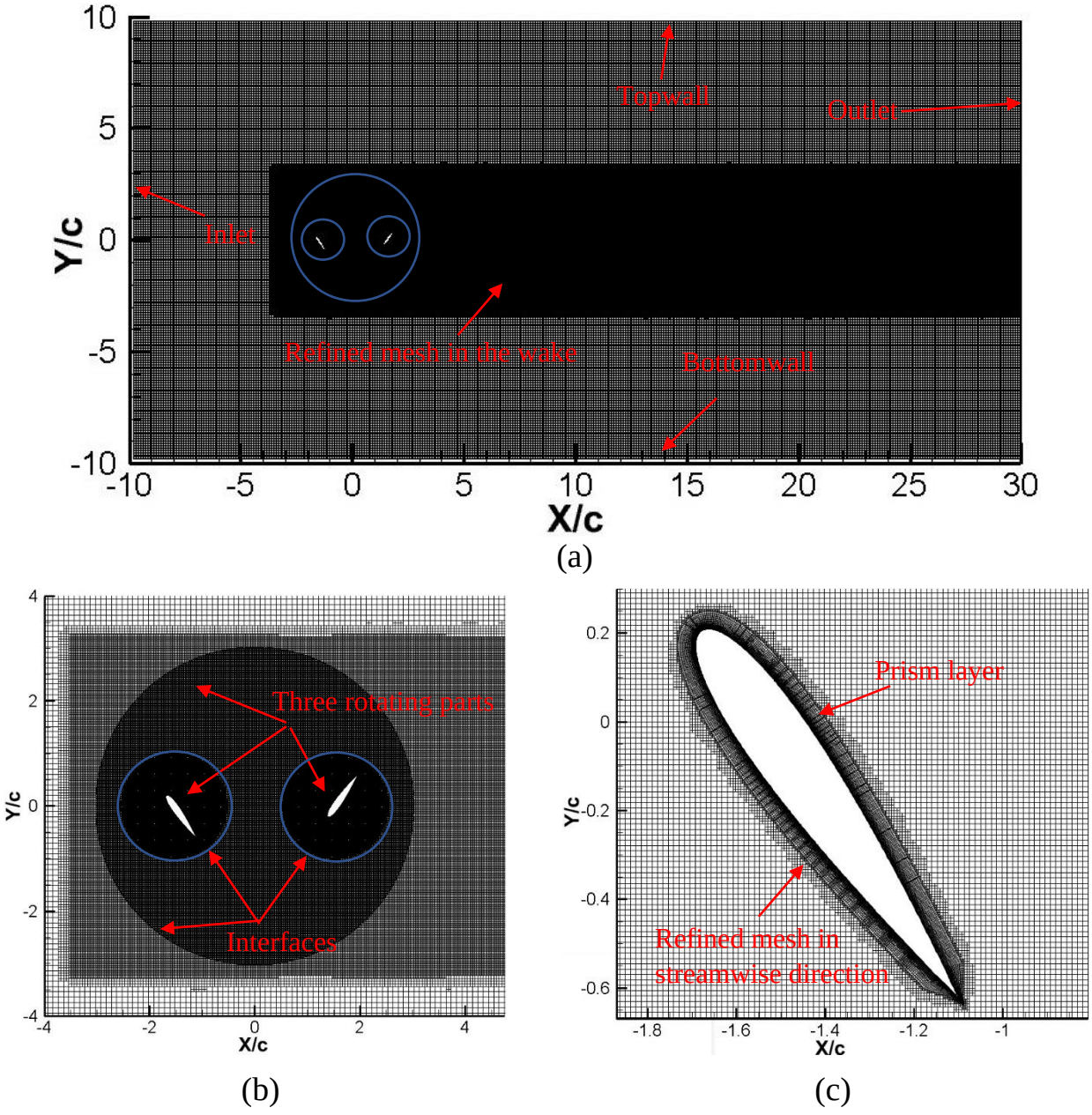

(a)

(b)

(c)

Fig.2 Computational configuration and mesh distributions. (a) Mesh in computational domain; (b) Mesh in three rotating parts; (c) Mesh near the blade surface.

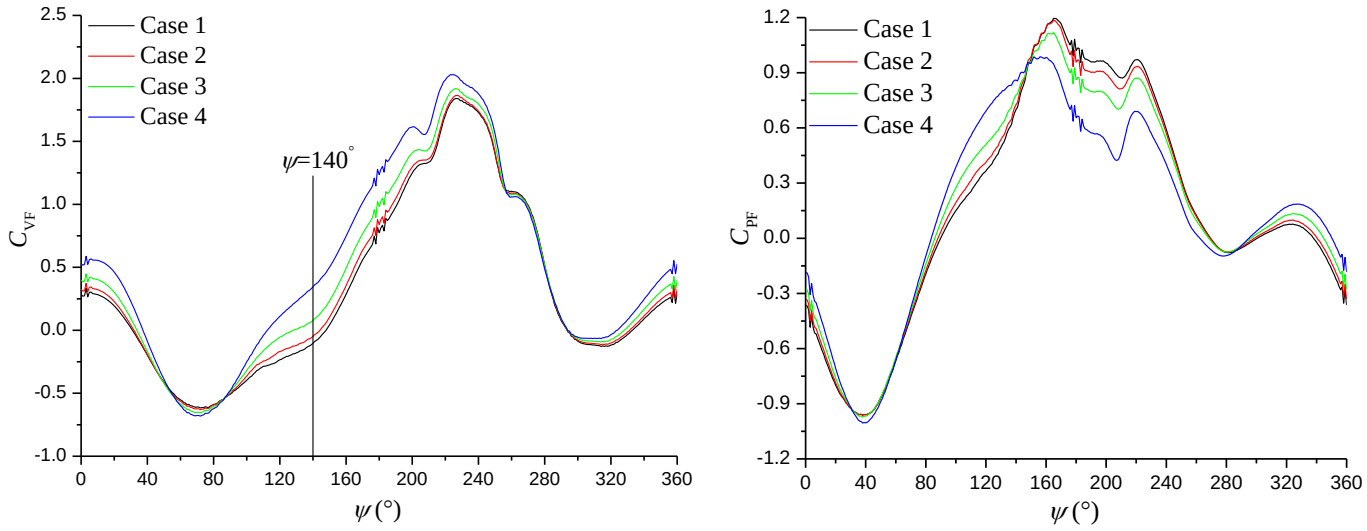

(a) (b)

Fig.3 Instantaneous performance of one blade in a revolution. (a) Vertical force coefficient; (b) Propulsive force coefficient.

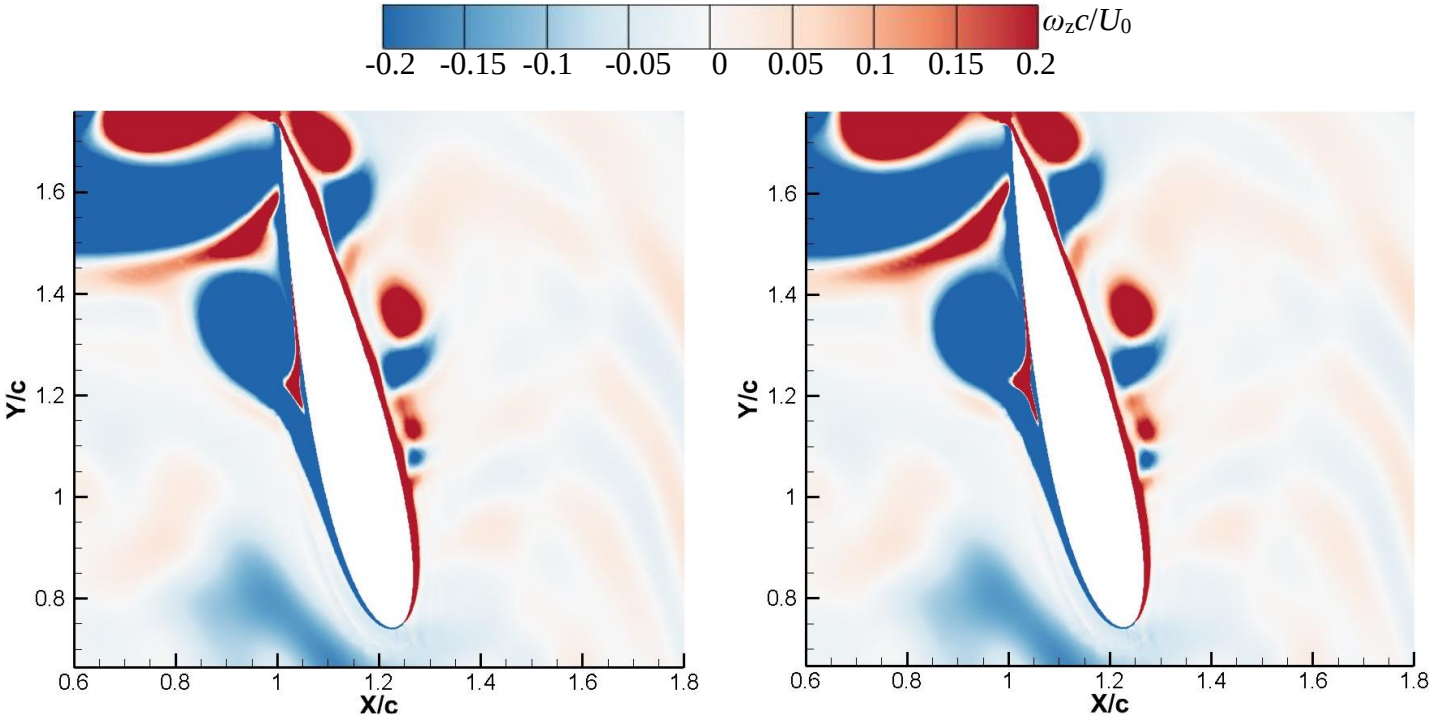

(a) (b)

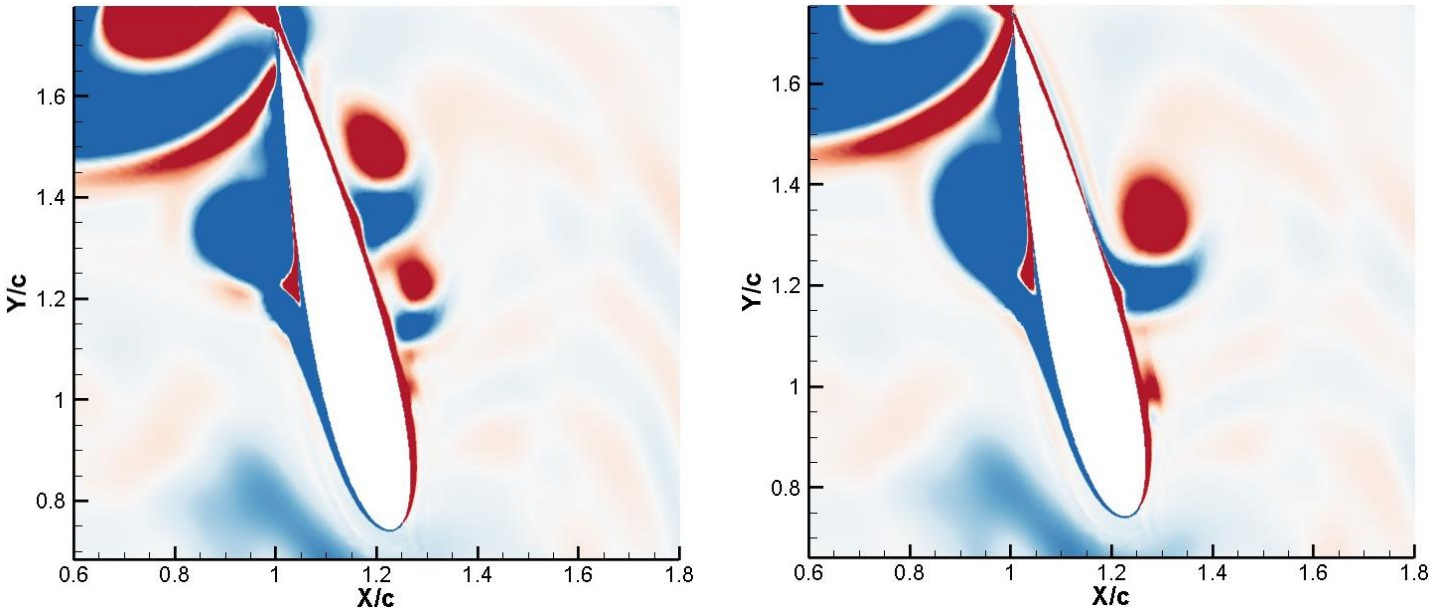

(c) (d)

Fig.4 Spanwise vorticity contours at ψ=140°. (a) Case 1; (b) Case 2; (c) Case 3; (d) Case 4.

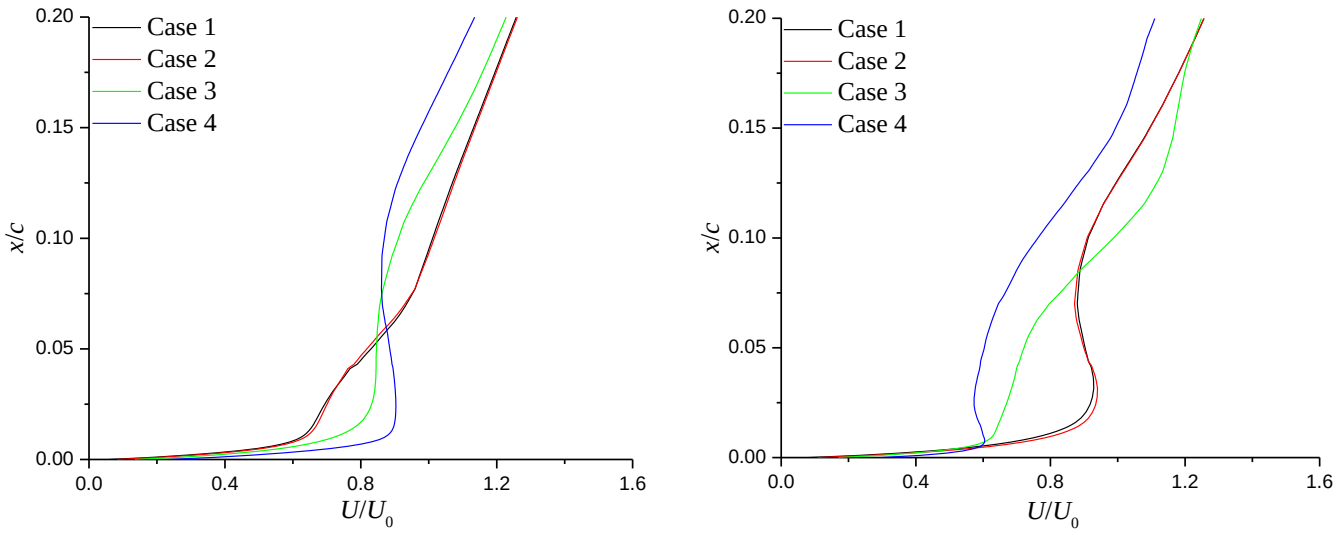

(a) (b)

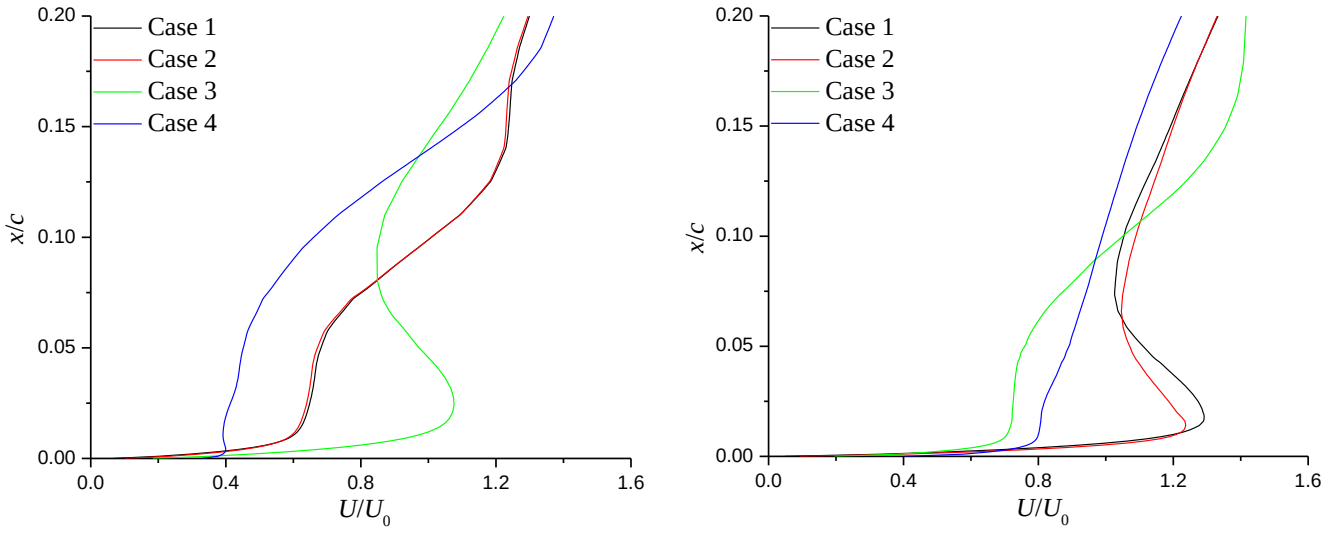

(c) (d)

Fig.5 Velocity profiles at ψ=140°. (a) y/c=0.4; (b) y/c=0.5; (c) y/c=0.6; (d) y/c=0.8.

3.3 Boundary conditions and numerical parameters

When given the boundary conditions, the classical one, velocity imposed on the inlet section and pressure assigned on the outlet part, is applied to the present computations. The top-wall and bottom-wall are set as symmetry planes to eliminate the sidewall effect. The blade surface is treated as no-slip wall condition. The finite-volume-based segregated flow solver is utilized to simulate the unsteady vortical flows. In the simulations, the second-order upwind spatial discretization is used for the convective flux and the second-order central discretization is employed to the diffusion term. The previous studies show that the freestream turbulence level has great impact on the transition [6-7]. In this work, the inflow turbulence intensity of 0.25% is chosen, which is consistent with the experimental measurement [28]. Simultaneously, the influence of the eddy viscosity ratio μ_t/μ (μ_t is the eddy viscosity and μ is the dynamic viscosity of the working fluid) is tested. In figure 6, on basis of the instantaneous vertical force and propulsive force coefficients in the last revolution, it seems that the results stay same as the eddy viscosity ratio changes from 10 to 0.01, but a little difference when it decreases to 0.001. It is reasonable to choose a low value of eddy viscosity ratio because of relatively low Reynolds number. Gauthier et al. [30] and Kinsey and Dumars [31] analyzed the unsteady flows around tandem oscillating hydrofoils of the hydrokinetic turbine, with the eddy viscosity ratio of 0.001 at Reynolds number 5×10^5. In addition, the propulsive force of the cycloidal rotor has a slight improvement when μ_t/μ=0.001 is selected.

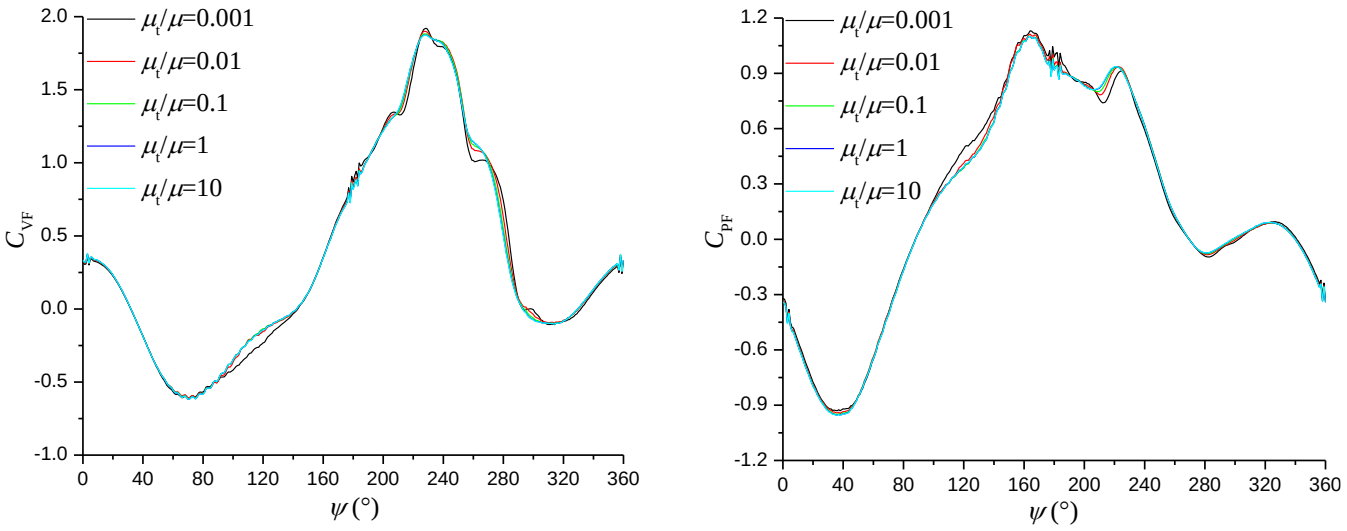

(a) (b)

Fig.6 Instantaneous performance of one blade in a revolution. (a) Vertical force coefficient; (b) Propulsive force coefficient.

The time-step, which has a close relationship with the simulation stability, has also remarkable influence on the numerical accuracy. The instantaneous vertical force and propulsive force coefficients of a single blade in the last rotating cycle are displayed in figure 7. Compared with the smallest one, using a relatively large value of time-step leads to a large discrepancy of the performance in some regions, for examples, vertical force coefficient at ψ=280°~340° and propulsive force coefficient at ψ=160°~220°. However, when the time-step is 0.5°, there are some large flow oscillations and the global performance has a slight decrease because of the more complicated vortical flows. Therefore, the time-step of 1° is adopted with the consideration of the computational resources and numerical stability.

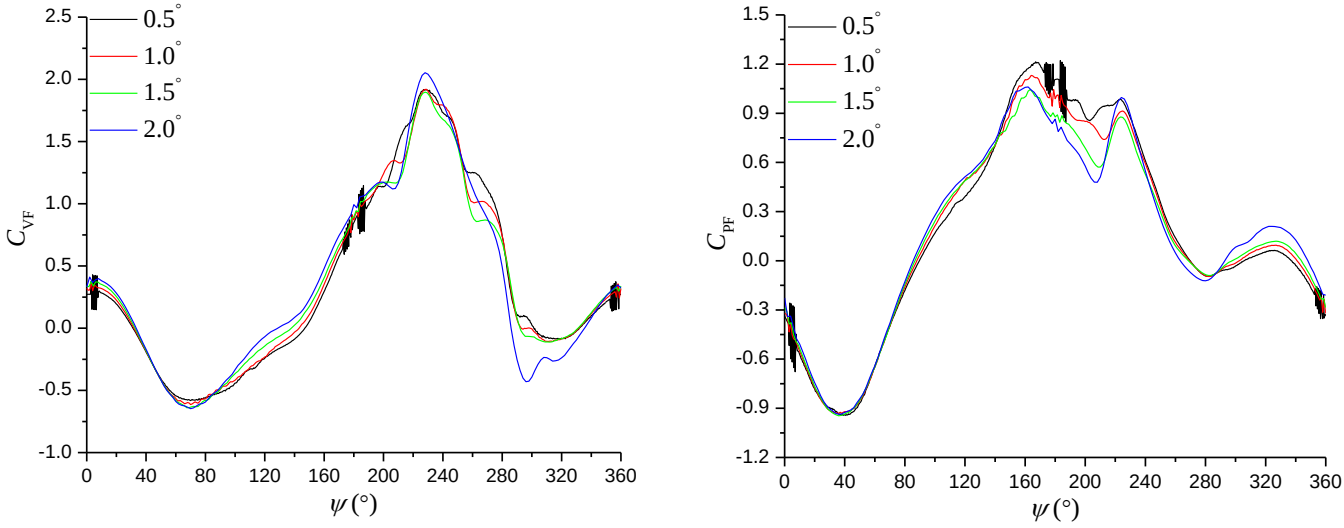

(a) (b)

Fig.7 Instantaneous performance of one blade in a revolution. (a) Vertical force coefficient; (b) Propulsive force coefficient.

The selection of the convergence target is also essential to the numerical accuracy. The effect of different convergence-iteration loops on the performance of a single blade is displayed in figure 8. It is observed that the iteration loop of 30 has an overprediction/underprediction of the instantaneous performance in some regions, for instances, at ψ=100°-140° and ψ=160°-220°. Then, if the iteration loop reaches to a value of 50, the convergence target has no evident influence on the results. Thus, the combination of 10^{-4}-50 is adopted in all the cases.

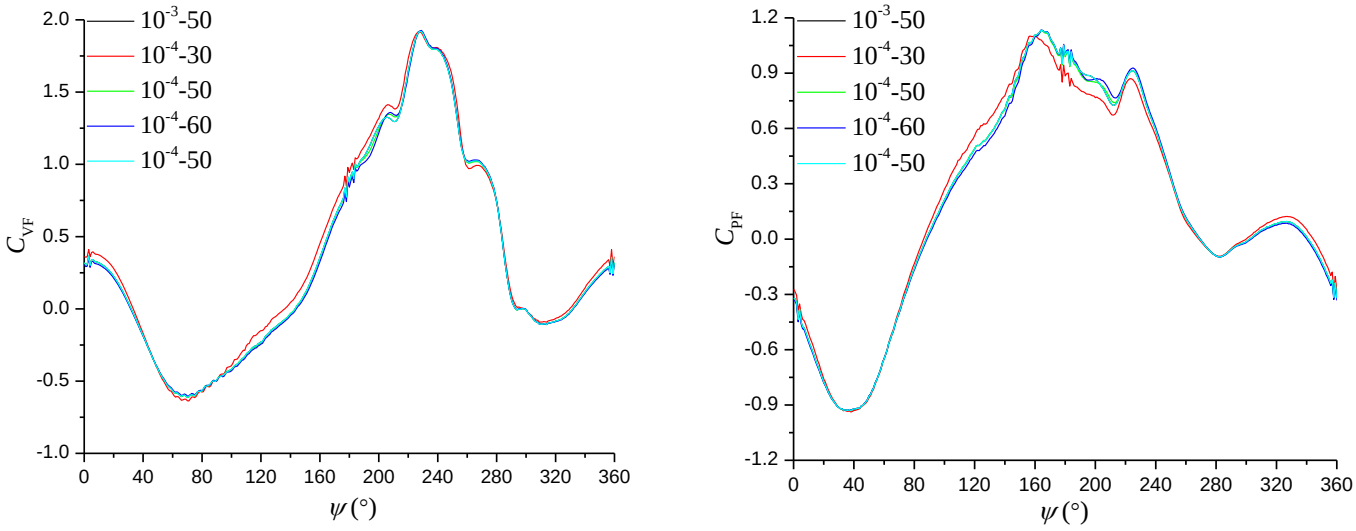

Fig.8 Instantaneous performance of one blade in a revolution. (a) Vertical force coefficient; (b) Propulsive force coefficient.

The other points that should be paid attention to are the use of wall function and numerical convergence. The all y^+ wall treatment is used in the current work, for the reason that it combines the low y^+ wall treatment for the fine mesh and high y^+ wall treatment for the coarse mesh. In addition, it also has reasonable answers for intermediate mesh which falls within the buffer region of the boundary layer. As a consequence, it is suitable for a wide range of near-wall mesh densities. Actually, it proves that there is no distinction in performance achieved by low y^+ and all y^+ wall treatments. Moreover, the maximal y^+ does not exceed the value of 0.5 at any locations in a rotating cycle. What is more, in unsteady computations, 15 rotations are necessary to get a periodic result, as shown in figure 9. Both the vertical force and propulsive force coefficients in last 5 rotations show no difference.

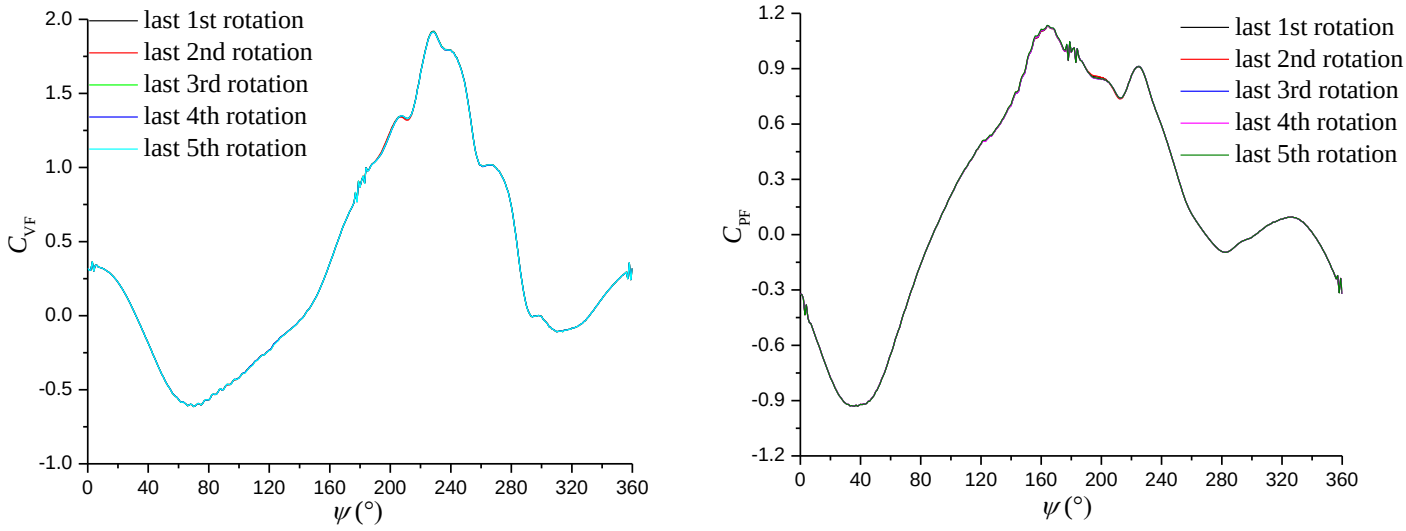

(a) (b)

Fig.9 Instantaneous performance of one blade in last 5 cycles. (a) Vertical force coefficient; (b) Propulsive force coefficient.

4. Results and discussion

4.1 Analysis of unsteady flow structures

The computational results, including the time-averaged lift, propulsive force, power and calculated efficiency of the cycloidal rotor, are displayed in Table 3 for different turbulence models, at two λ. The efficiency is defined as $\eta=(-F_x\times U_0)/P$ (F_x is negative propulsive force and P is the power). At λ=0.52, the lift, propulsive force and efficiency obtained by SST γ-$Re_{\theta t}$ transition model (SST TM) are very close to the experiments. The power predicted by different turbulence models is always lower than the experimental measurement, largely induced by the neglect of the power consumption of the shaft and other mechanical components. In addition, although the produced power shows a good agreement with the experimental value, the Reynolds stress model (RSM) underpredicts the lift and overpredicts the propulsive force. Then, when λ is 0.73, both the SST k-ω model and SST TM underpredict the propulsive force because of its small value, but the power and efficiency obtained by SST TM has relatively small discrepancy compared with the experiments.

Table 3 Results of different turbulence models

λ=0.52	Lift (N)	Propulsive force (N)	Power (W)	Efficiency (%)
Laminar model	0.574	0.181	2.517	35.96
Spalart-Allmaras (SA) model	0.485	0.187	2.032	46.01
Realizable k-ε model	0.588	0.234	2.299	50.89
SST k-ω model	0.475	0.236	2.823	41.80
SST TM	0.494	0.247	3.136	39.38
RSM	0.469	0.306	3.408	44.89
EXP	0.49	0.26	3.55	36.6
λ=0.73				
SST k-ω model	0.619	-0.0566	1.44	-27.49
SST TM	0.614	-0.00489	1.99	-1.72
EXP	0.64	0.06	2.50	16.8

The instantaneous vertical force, propulsive force and power coefficients ($C_{power}=P/(0.5*\rho*U_0^3*c$, where P is the power) of the single blade for three turbulence models, namely SST k-ω model, SST TM and RSM, are plotted in figure 10 at two λ. The performance obtained by RSM is only presented at λ=0.52 and the results show a noticeable fluctuation, which is owing to the disordered flow structures caused by resolving more equations in RSM with fine mesh and small timestep. The present work is also compared with the existing computational results using SA γ-$Re_{\theta t}$ transition model (SA TM) [28]. At two λ, it is observed that the large difference of the performance occurs in the lower half cycle when the blade is undergoing the advancing side, which may be due to the choice of turbulence model and the numerical solver. The critical locations where the values of forces and power have the transition, are listed in table 4 for different turbulence models. It concludes that increasing λ has no obvious effect on the force production regions, but has little influence on the peaks of these variables. Besides, it seems that the results of the single blade obtained by the SST k-ω model and SST TM have no evident difference, which is presented in figure 10.

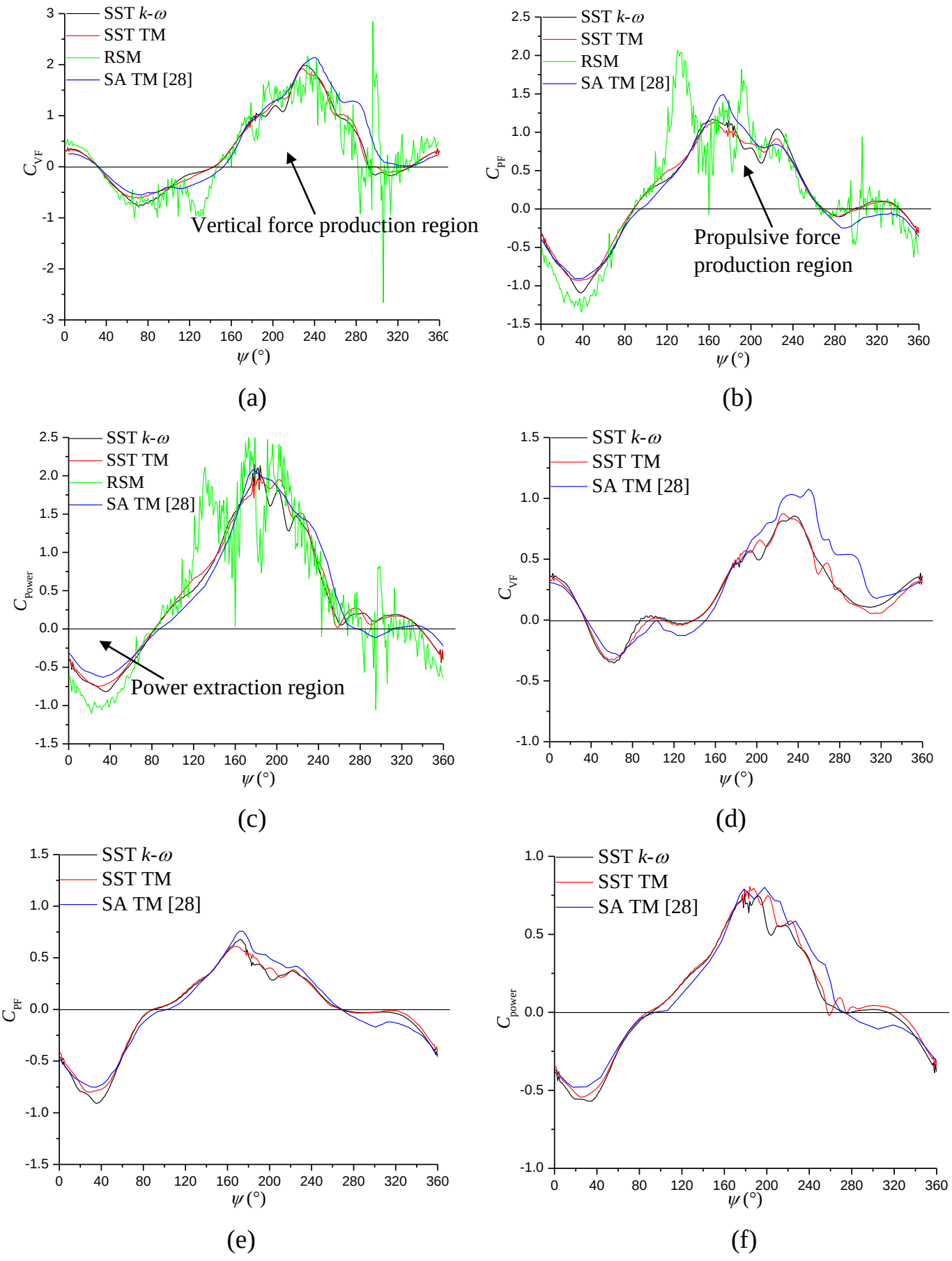

Fig.10 Instantaneous vertical force, propulsive force and power coefficients of single blade in a revolution at two λ. (a), (b) and (c) at λ=0.52; (d), (e) and (f) at λ=0.73.

Figure 11 shows the forces (lift and drag) acting on one blade at different ψ when λ is 0.52. At ψ=32°, the blade is nearly vertical and it is experiencing the retreating side. At this moment, the components of lift and drag generated in the positive X axis leads to the production of the large negative propulsive force, which is shown in figure 10b. However, the component of the lift is almost balanced by the component of the drag in Y axis. Consequently, the vertical force on this blade approaches to zero. This situation is quite similar with that at ψ=144°, but the components of lift and drag in negative X axis are responsible for the creation of the large positive propulsive force. For the propulsive force transition, the critical moment is when the blade is almost located at ψ=90° and ψ=270°. At these two positions, the lift F_L provides the vertical force of the blade totally, but the direction is contrary, as shown in figure 10a. Simultaneously, the drag F_D makes the contribution to the propulsive force at ψ=90° and 270°, but its magnitude is extremely small because the relative attack-of-angle is nearly equal to zero.

Table 4 Main production regions of forces and power

λ=0.52	Negative vertical force region (°)	Positive vertical force region (°)	Negative propulsive force region (°)	Positive propulsive force region (°)	Negative power region (°)	Positive power region (°)
SST *k-ω*	32-144	144-360	0-89	89-269	0-83	83-338
SST TM	32-144	144-360	0-89	89-269	0-83	83-338
SA TM [28]	32-153	153-360	0-96	96-267	0-87	87-344
λ=0.73						
SST *k-ω*	34-140	140-360	0-90	90-269	0-92	92-312
SST TM	34-140	140-360	0-90	90-269	0-88	88-323
SA TM [28]	36-151	151-360	0-103	103-269	0-100	100-272

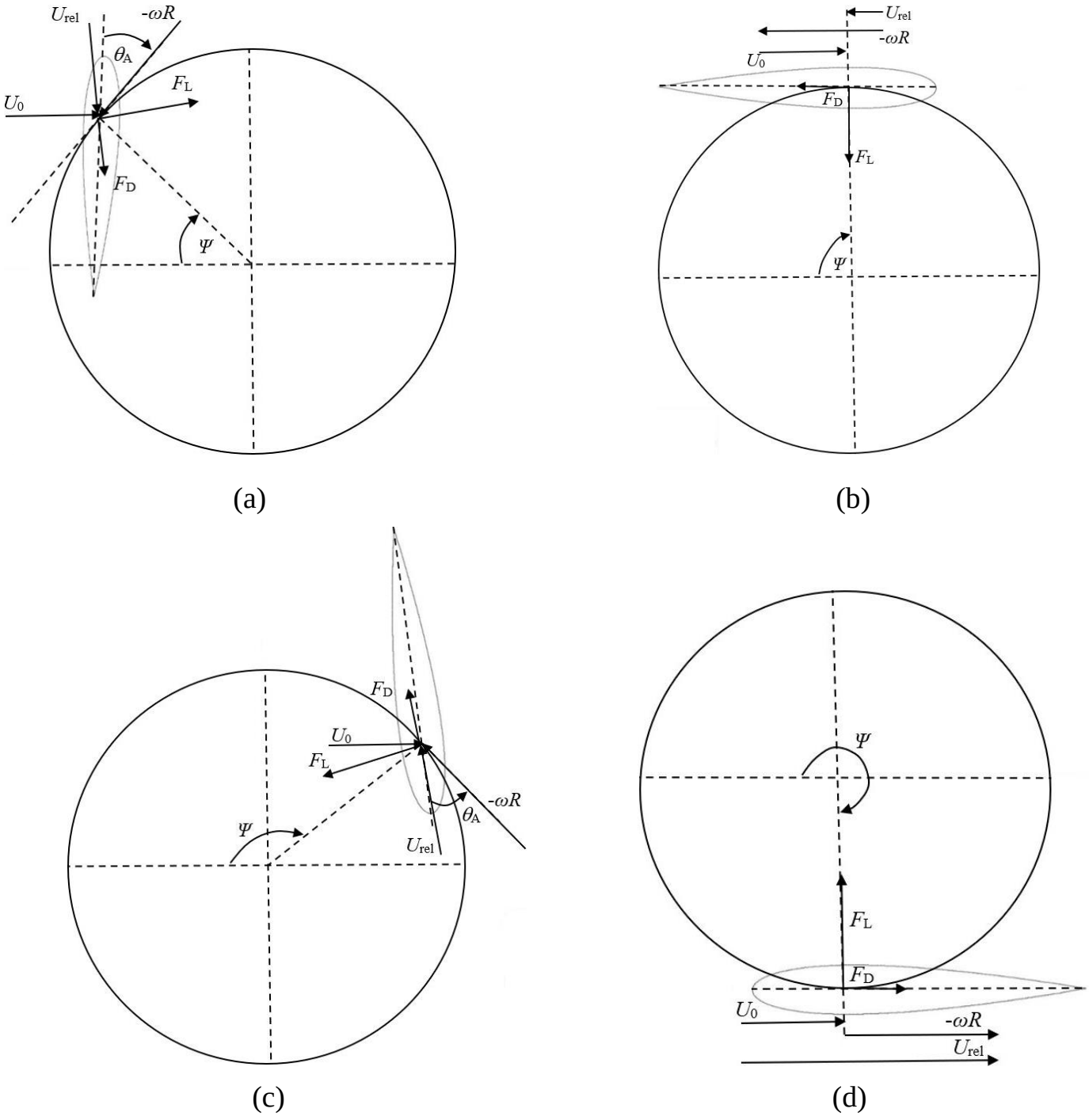

Fig.11 Sketch of forces acting on one blade at different ψ. (a) ψ=32°; (b) ψ=90°; (c) ψ=144°; (d) ψ=270°.

The detailed flow structures achieved by two turbulence models, including the velocity and vorticity contours, are shown in figure 12 at ψ=0° when λ is 0.52. The numerical simulations are compared with the experimental measurements [28]. At this instant, both two blades have the largest relative incidence. Compared with the experiments, it seems that the present computation can capture the gross feature of the internal flow structures, such as the trajectory of wakes shedding from two blades and the interaction of blade B with its own wake. By the comparison of velocity and vorticity distributions, it is observed that the vortical flows dissipate quickly for SST

TM, particularly in the wake region, which infers that the earlier onset of vortex shedding due to the susceptibility of disturbances. To clarify the difference of near-wall flows for two turbulence models, the pressure coefficient C_p ($C_p=p/(0.5\times\rho\times U_0^2)$, where p is the pressure) and relative velocity contours of blade B are plotted in figure 13. Based on the pressure distributions, it is observed that there is almost no difference for blade A, but has evident dissimilarity for blade B, especially near the leading edge (x/c=0~0.35) and the trailing edge (x/c=0.65~1.0) on the suction surface. The pressure difference near the leading edge is primarily due to the low-pressure region induced by the prediction of the stagnation point, but it recovers quickly at x/c=0.35. Then, downstream from x/c=0.65, the onset of boundary layer separation is evident, which is earlier and more violent for SST TM, causing the significant pressure degradation.

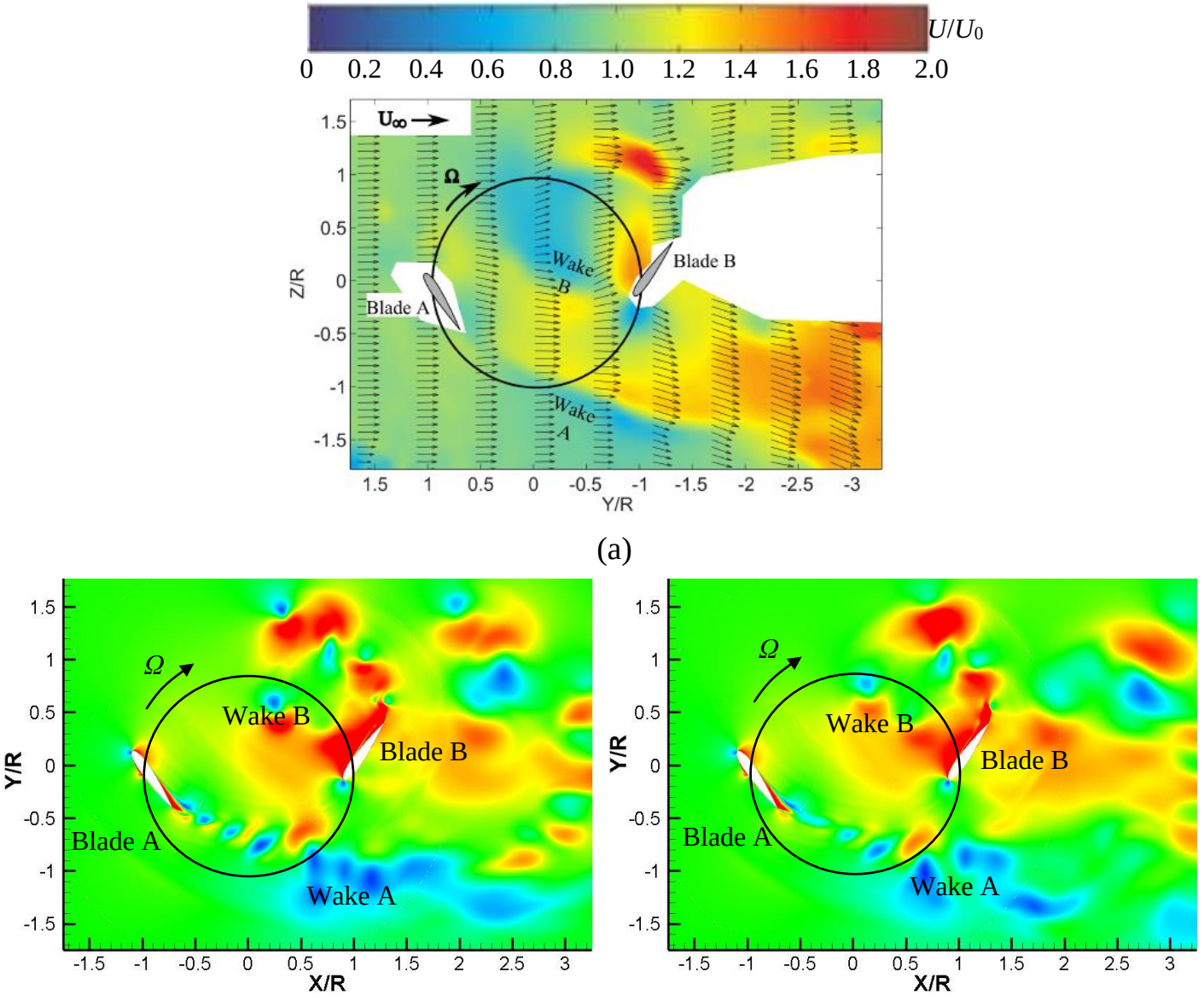

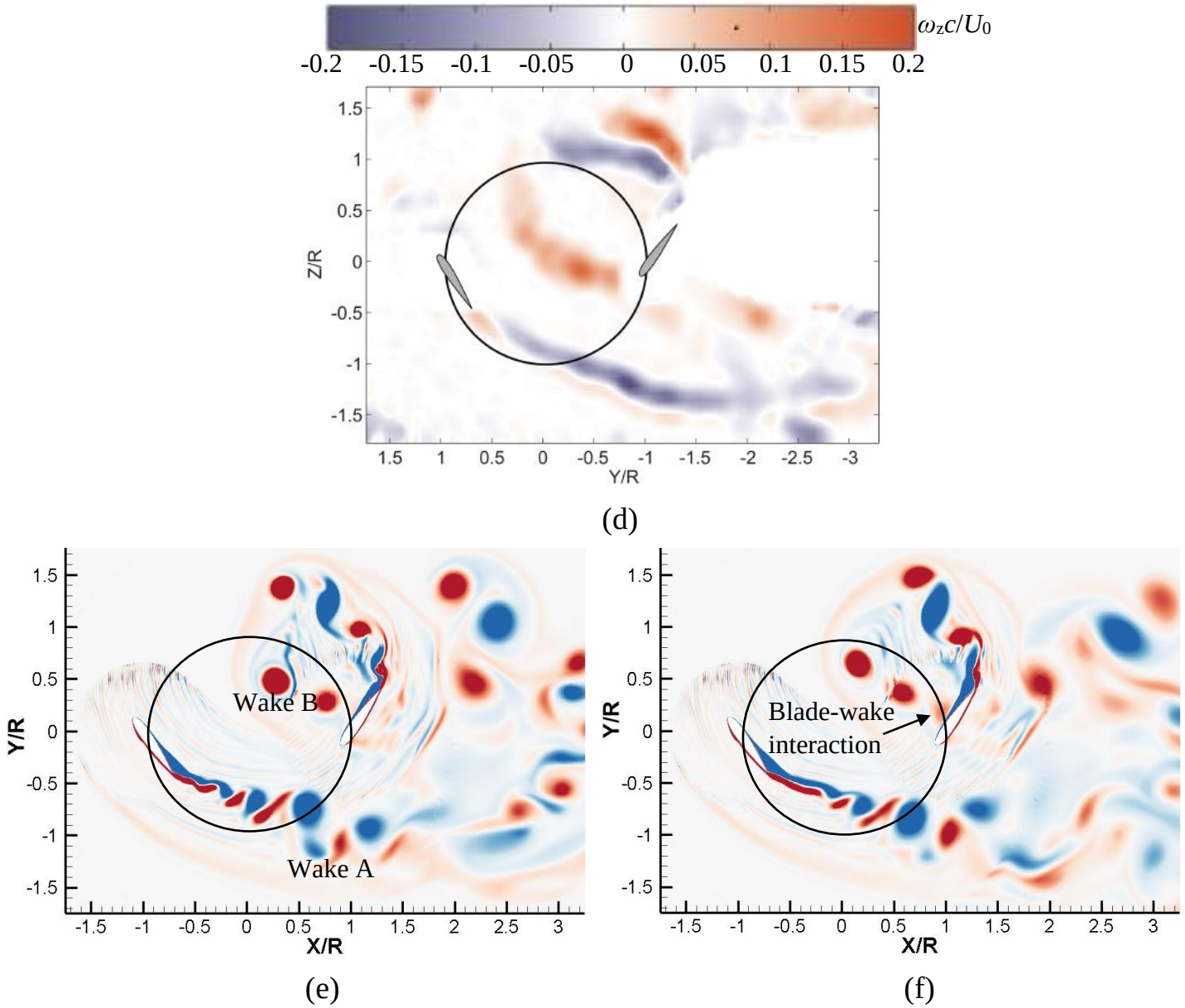

Fig.12 Velocity and vorticity contours. (a) and (d) Experiments; (b) and (e) SST *k*-ω; (c) and (f) SST TM.

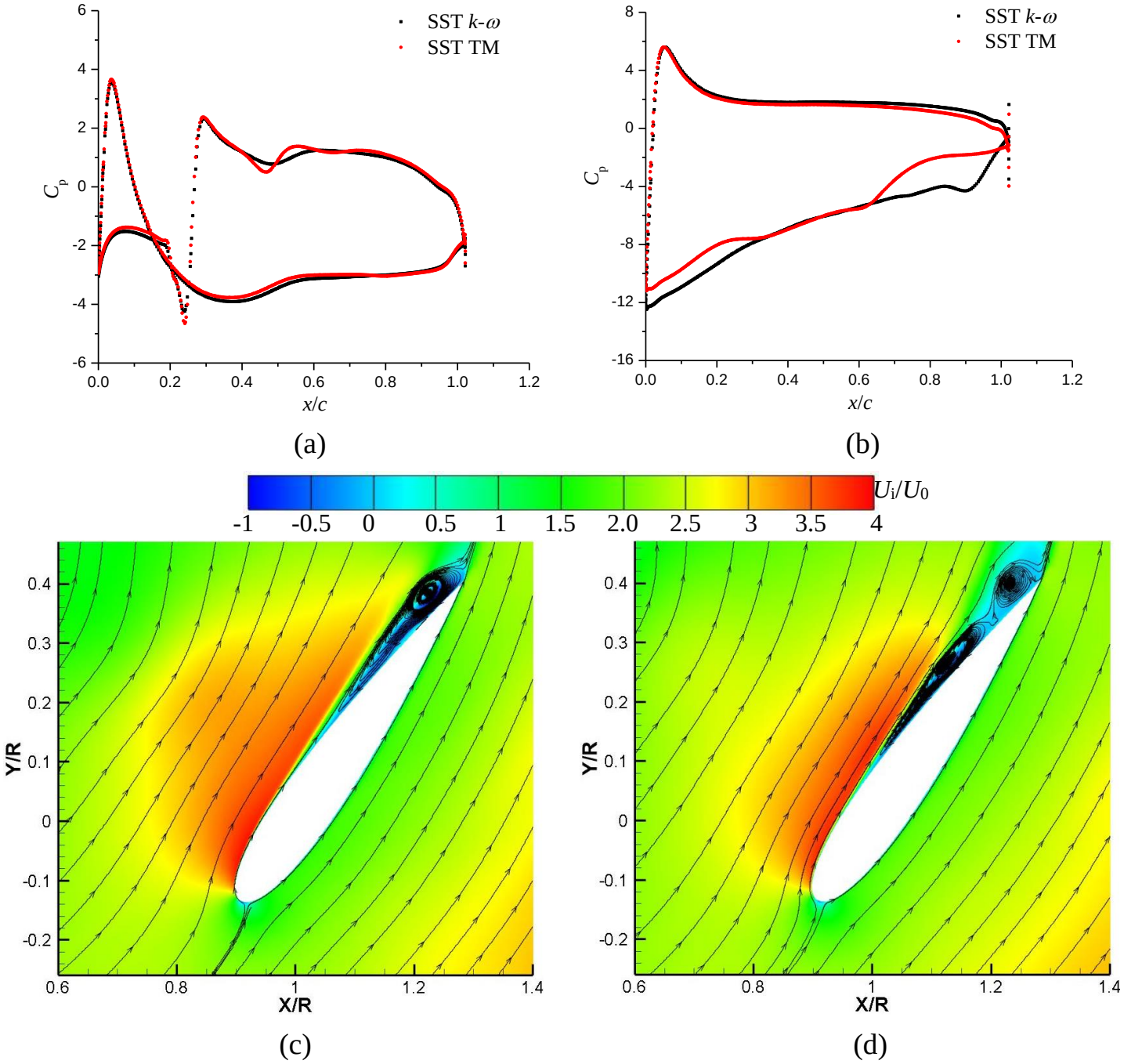

Fig.13 Pressure and relative velocity. (a) Pressure of blade A; (b) Pressure of blade B; (c) SST *k-ω*; (d) SST TM.

When ψ is 30°, the flow filed is more complicated than that at ψ=0°, shown by the distributions of velocity and vorticity contours in figure 14. It is obvious that the wake of blade A has a strong interaction with blade B, which is quite different from that in figure 12 where the blade B interacts with its own wake. In addition, the wake of blade B also has a strong interaction with wake B itself. Then, the detailed flow structures over two blades are displayed in figure 15, including the pressure coefficients, relative velocity contours and velocity profiles. For blade A, the main difference of the pressure predicted by two turbulence models is at x/c=0.25~0.5, due

to the existence of many small-scale vortices inside the boundary layer. Clearly, the SST TM resolves more scales near the wall, even a small vortex near the trailing edge causing the pressure drop on the pressure side, as shown in figure 15a. Afterwards, the flow over blade B is more complex. There are three obvious distinctions for two turbulence models: (1) the low-pressure region near the leading edge on the suction side; (2) the flow separation after the middle chord; (3) the high-pressure region near the leading edge on the pressure surface. The pressure difference near the leading edge both on two sides is as a result of the stagnation point deviation. Certainly, the blade-wake interaction also more or less leads to this difference. Near the blade trailing edge, the flow separation predicted by SST TM is more intensive, which has great impact on the blade loading. What is more, in figure 14e, 15e and 15f, it is found that the blade-wake interaction has a significant effect on the external flow filed near the leading edge, especially for SST *k-ω* model, presented by the velocity profiles near the leading edge of the pressure side, which are shown in figure 15g and 15h.

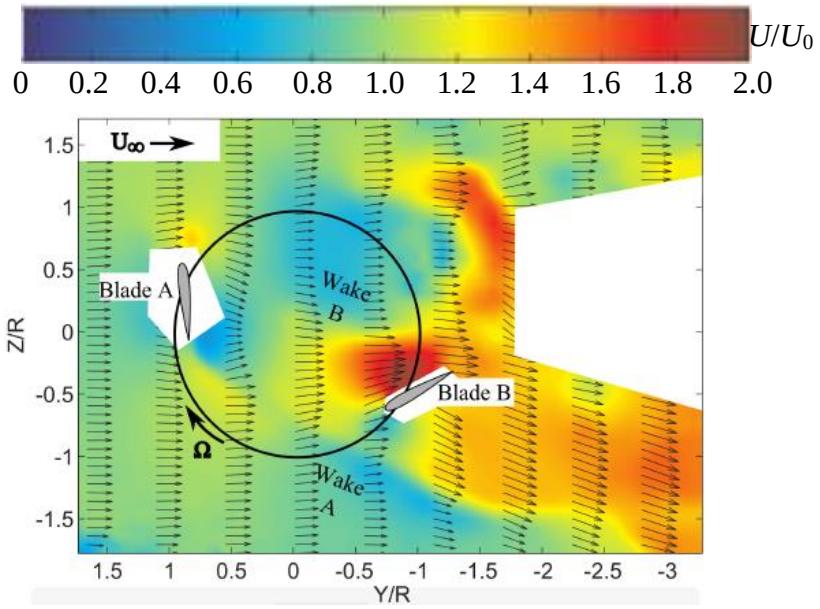

(a)

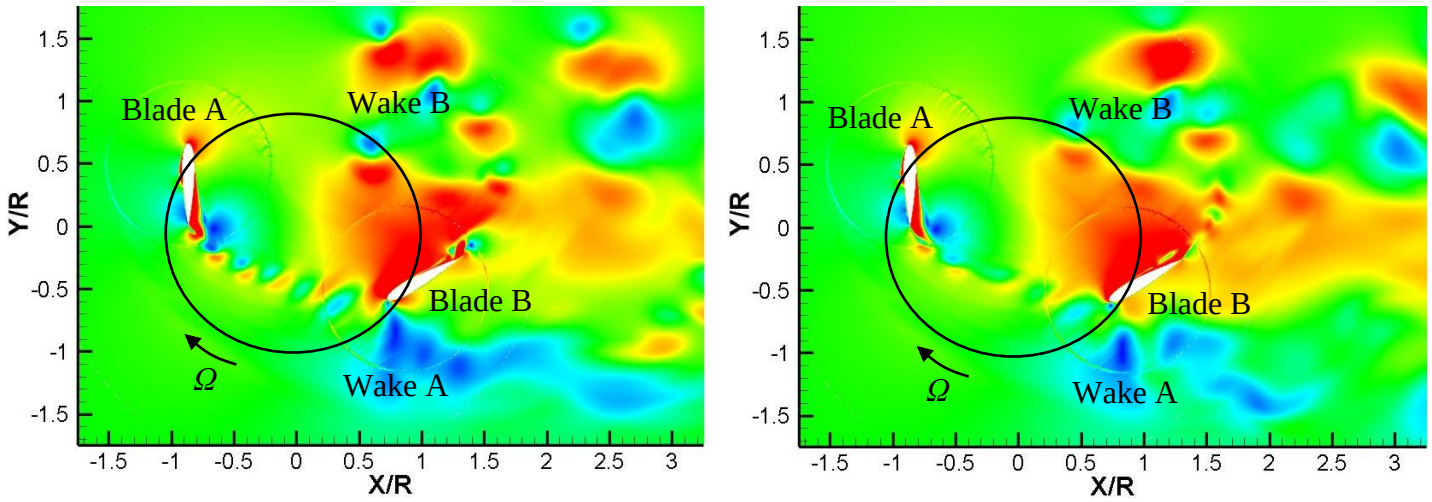

(b) (c)

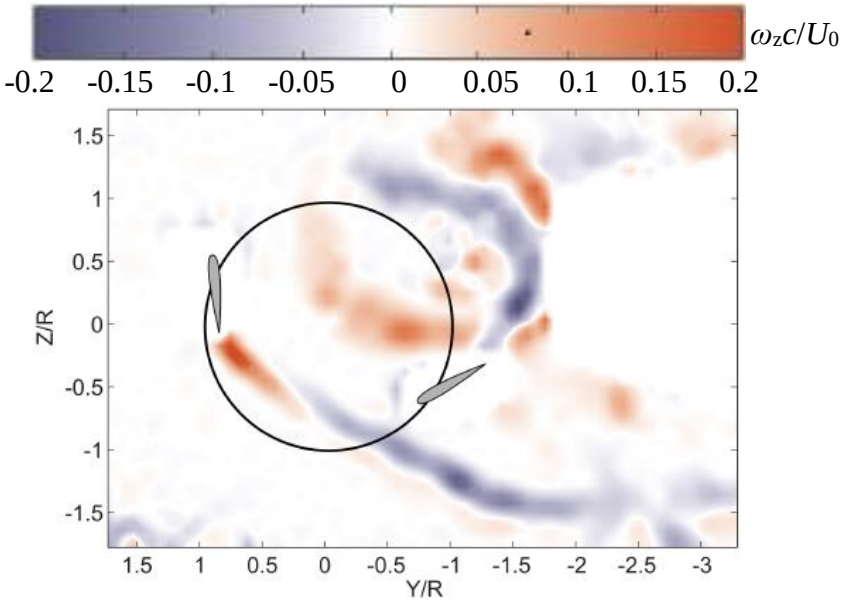

(d)

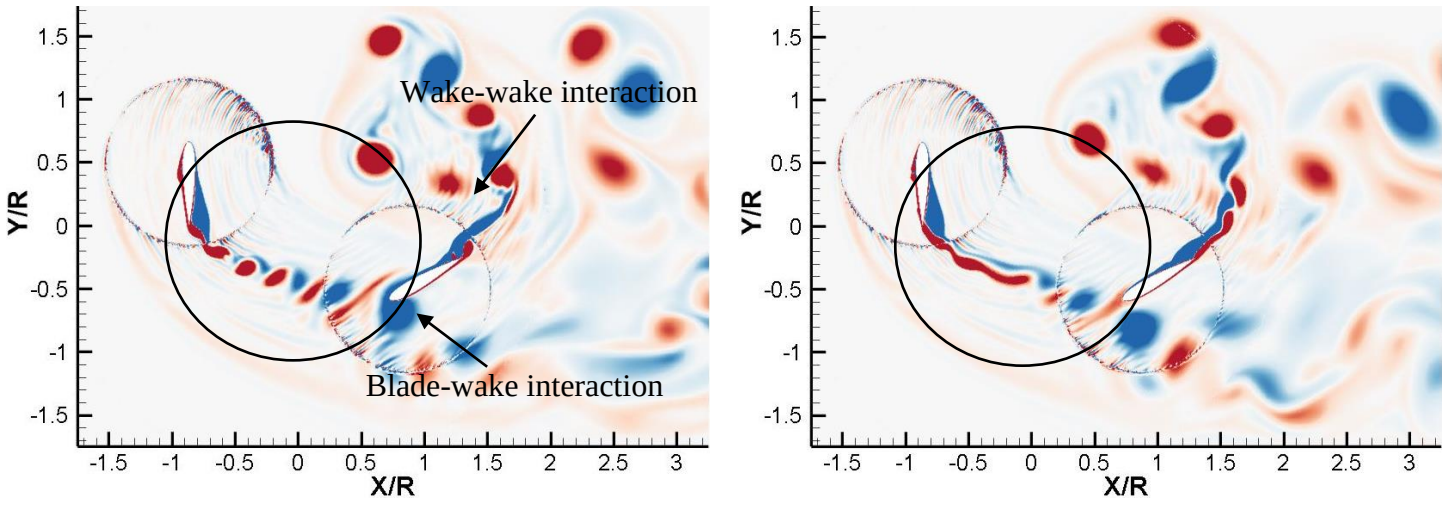

(e) (f)

Fig.14 Velocity and vorticity contours. (a) and (d) Experiments; (b) and (e) SST *k*-*ω*; (c) and (f) SST TM.

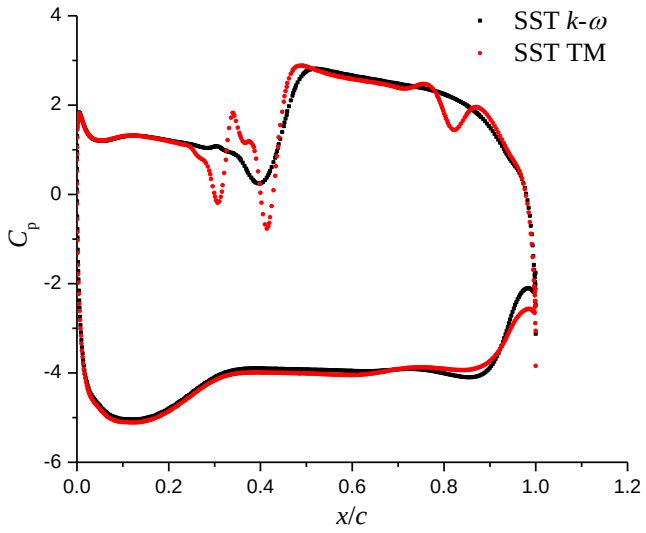
SST k-ω
SST TM
C_p
x/c

(a)

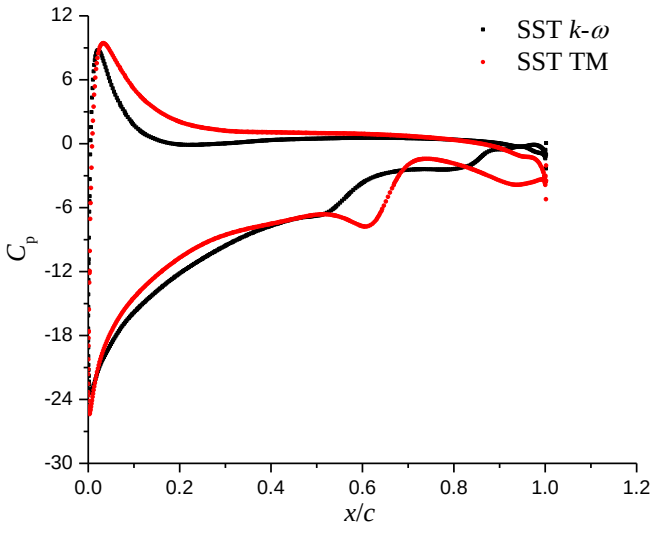
SST k-ω
SST TM
C_p
x/c

(b)

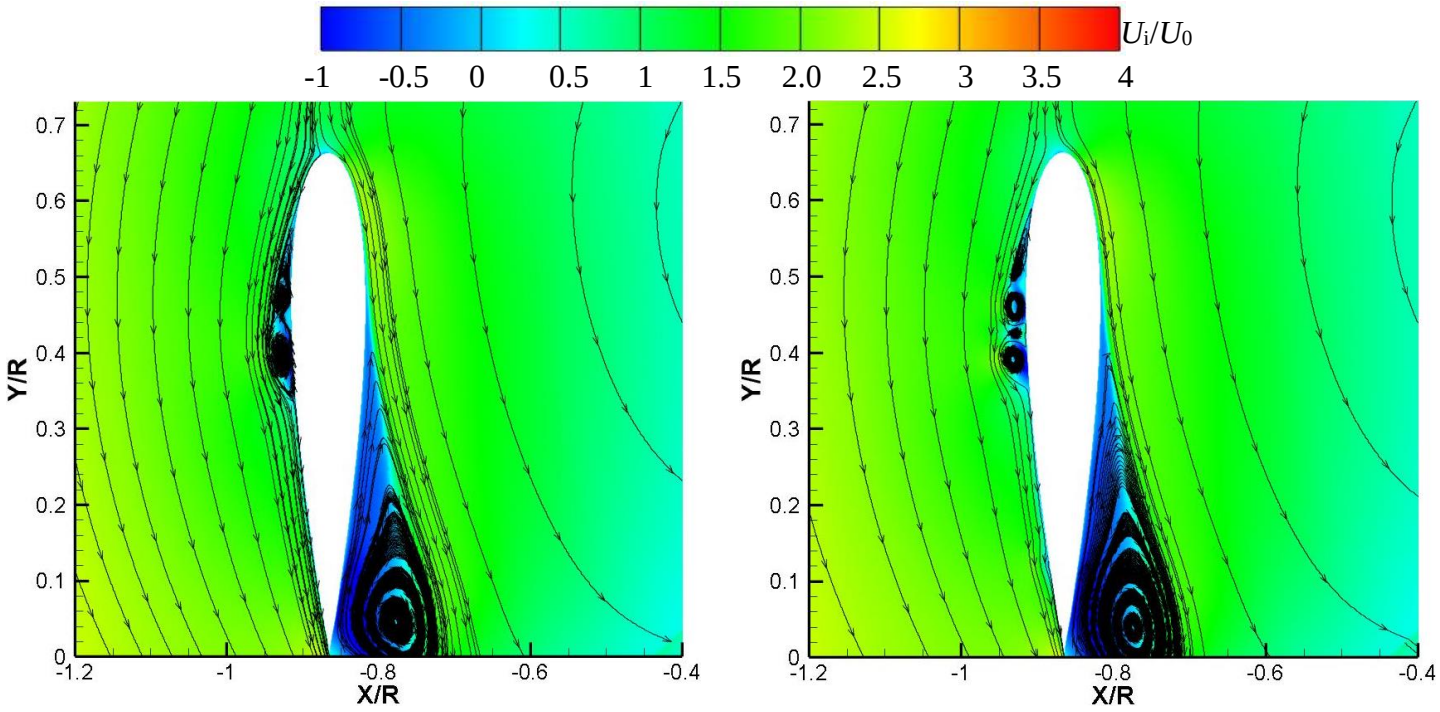
U_i/U_0
-1 -0.5 0 0.5 1 1.5 2.0 2.5 3 3.5 4
Y/R
X/R

(c)

(d)

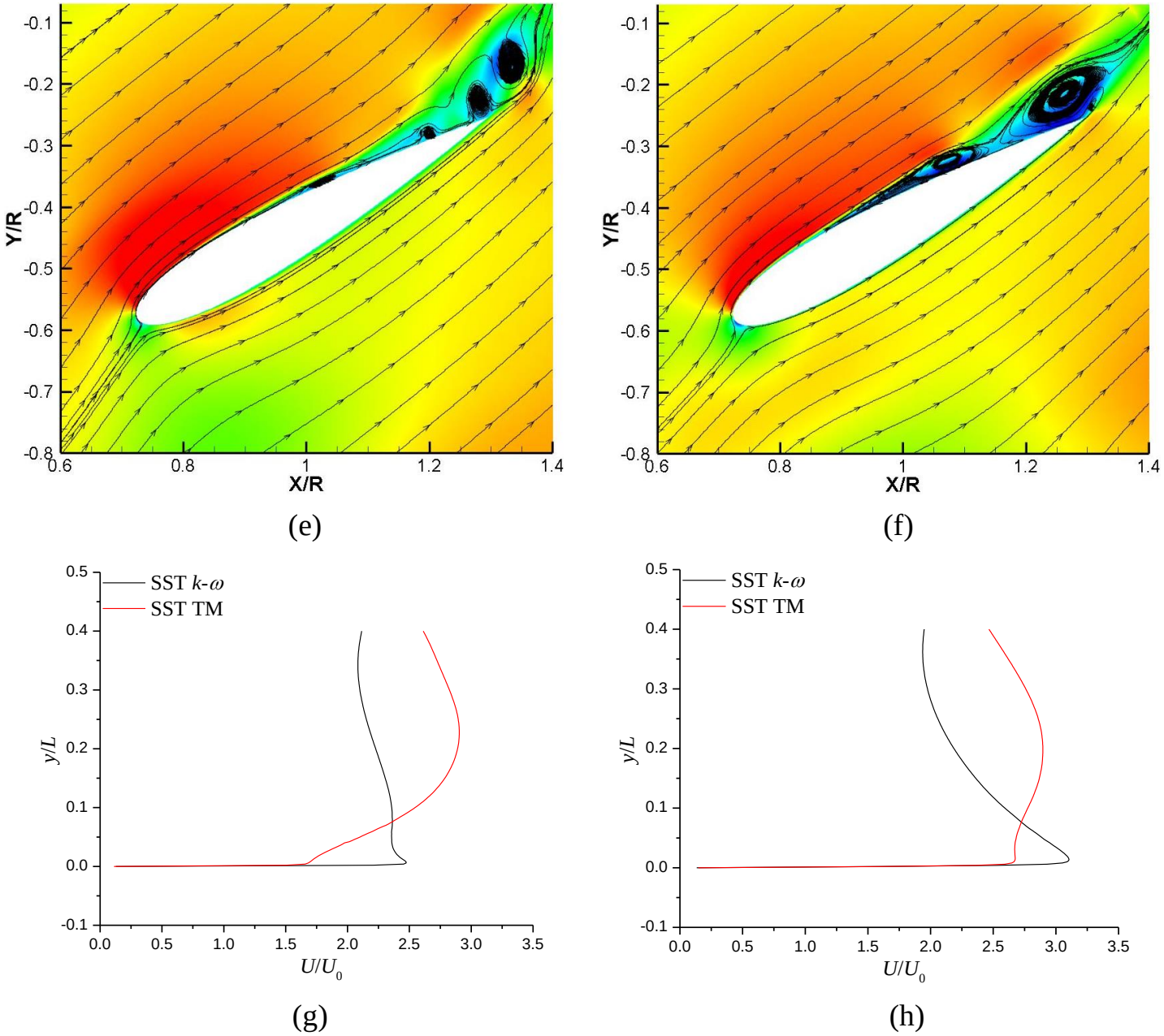

Fig.15 Pressure, relative velocity and velocity profiles. (a) Pressure of blade A; (b) Pressure of blade B; (c) and (e) SST k-ω; (d) and (f) SST TM; (g) Velocity profile of blade B at x/c=0.05 on the lower surface; (h) Velocity profile of blade B at x/c=0.1 on the lower surface.

In the next moment, at ψ=60°, blade B has already come across the wake shedding from blade A, but the wake A contacts with wake B near the trailing edge of blade B. Besides, the wake of blade B also has an interaction with itself, indicating a wake-wake interaction. The trajectory of wake shedding from blade A in the experiments has a little difference compared with the simulations, which impacts directly on the upper surface of blade B, as shown in figure 16d. However, the computations can still seize the gross feature of unsteady vortical flows. The detailed description of the flow field near the blade surface is shown in figure 17, using the pressure coefficients and velocity contours. The pressure of blade A predicted by

SST *k*-ω model has some difference compared with that obtained by SST TM, in regions where the small-scale vortex attaches on the pressure side and the flow separation emerges near the trailing edge of the suction side. At ψ=30°, the unstable area of the pressure on the pressure side is at x/c=0.25~0.5, but it extends to x/c=0.3~0.7 with the development of the attached vortex at ψ=60°. The SST TM resolves the discrete vortices inside the boundary layer, resulting in the pressure fluctuation, as shown in figure 17a. Near the trailing edge of the suction side, the pressure is greatly influenced by the large-scale flow separation vortex, especially for SST *k*-ω model. For blade B, the laminar separation bubble predicted by SST TM is formed near the leading edge. After LSB, the flow would reattach on the surface and then the turbulent boundary layer separation appears, shown in figure 17f. But the SST *k*-ω model only captures the fully turbulent boundary layer after a turbulent separation bubble, which will be discussed later in detail. Generally, it concludes that the considerable difference of the pressure on the suction side of blade B is due to the laminar-turbulence transition and turbulent boundary layer separation.

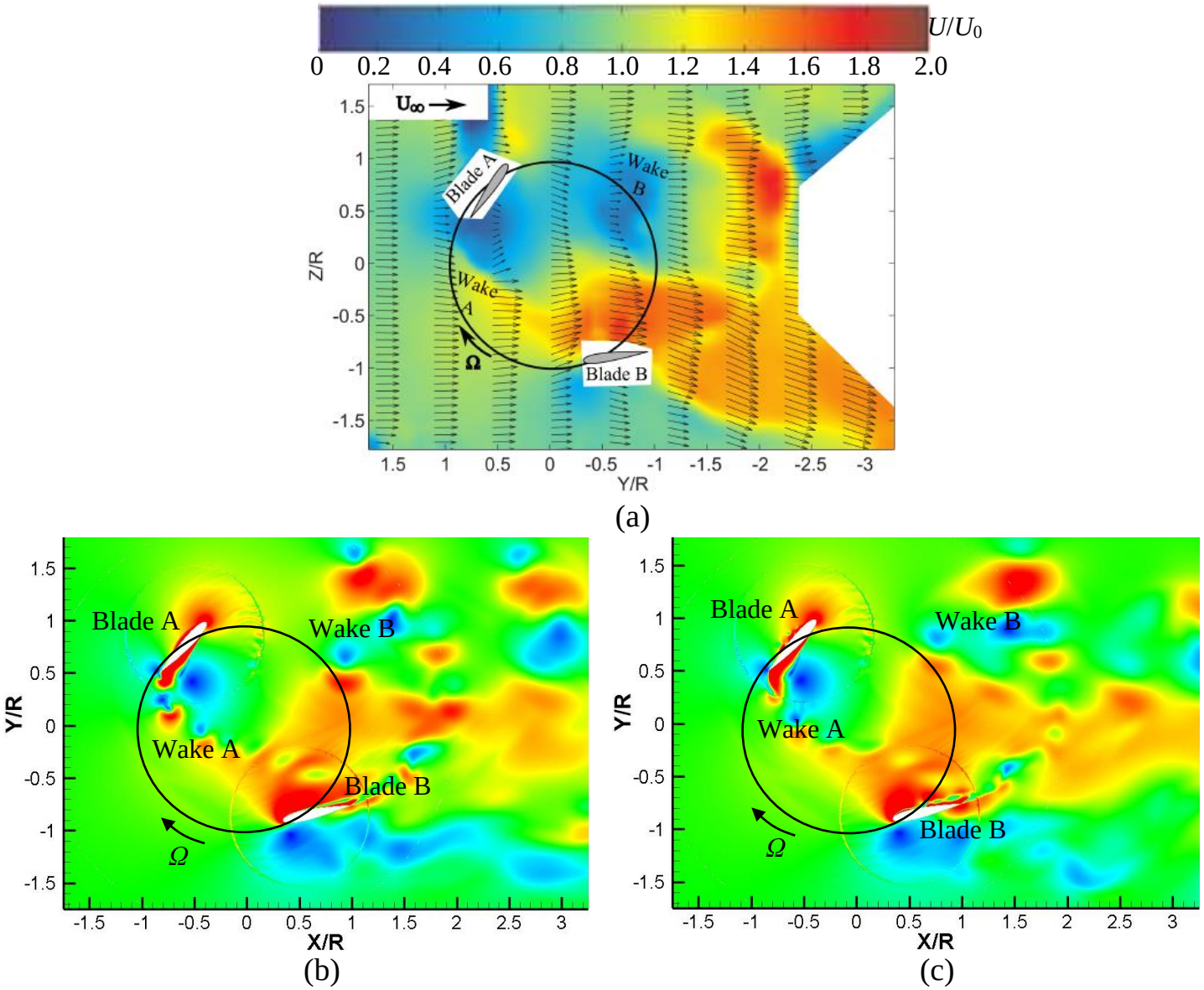

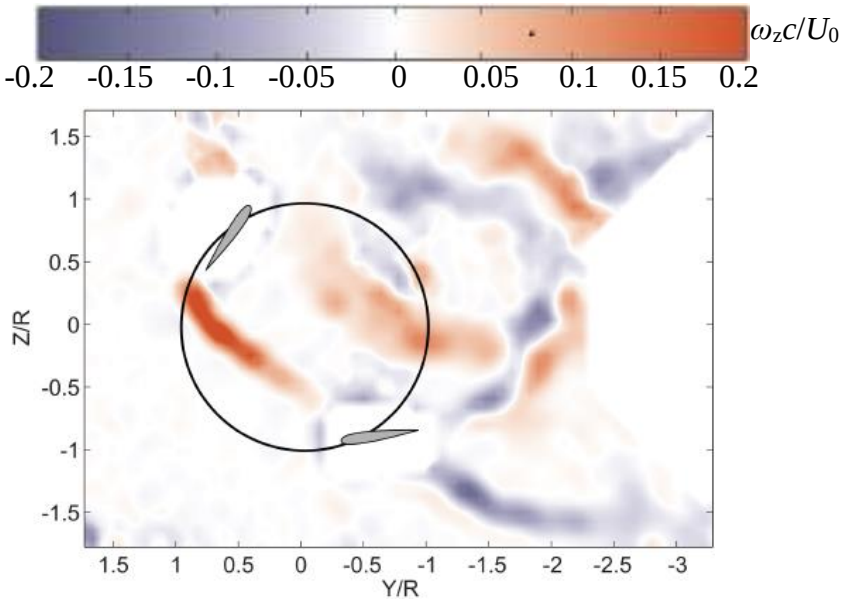

(d)

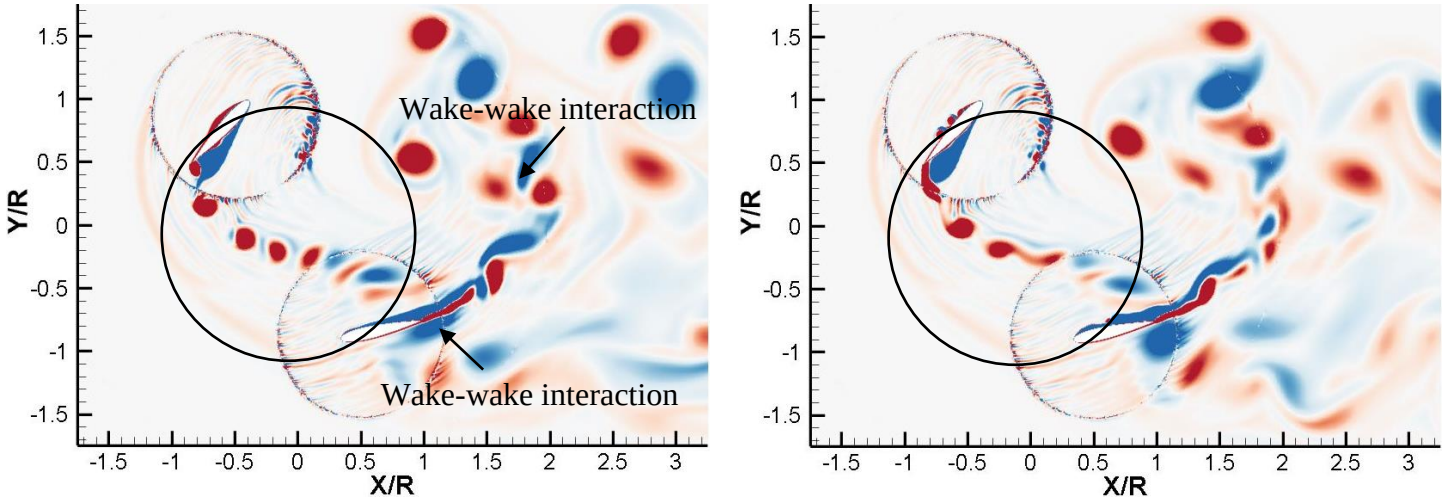

(e) (f)

Fig.16 Velocity and vorticity contours. (a) and (d) Experiments; (b) and (e) SST *k*-ω; (c) and (f) SST TM.

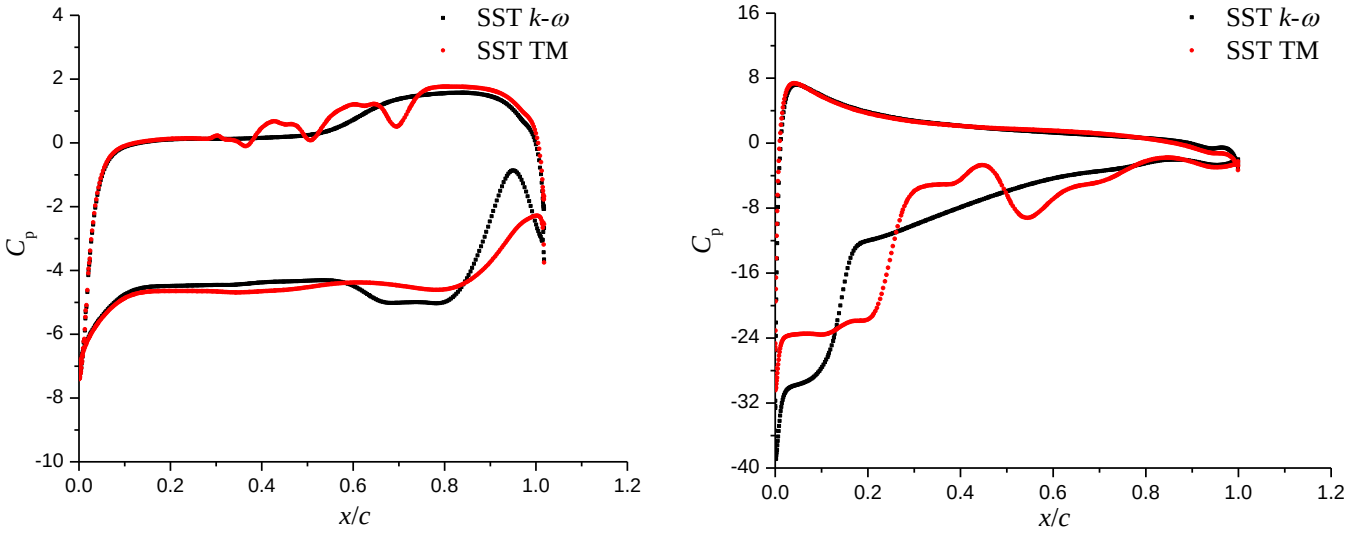

(a) (b)

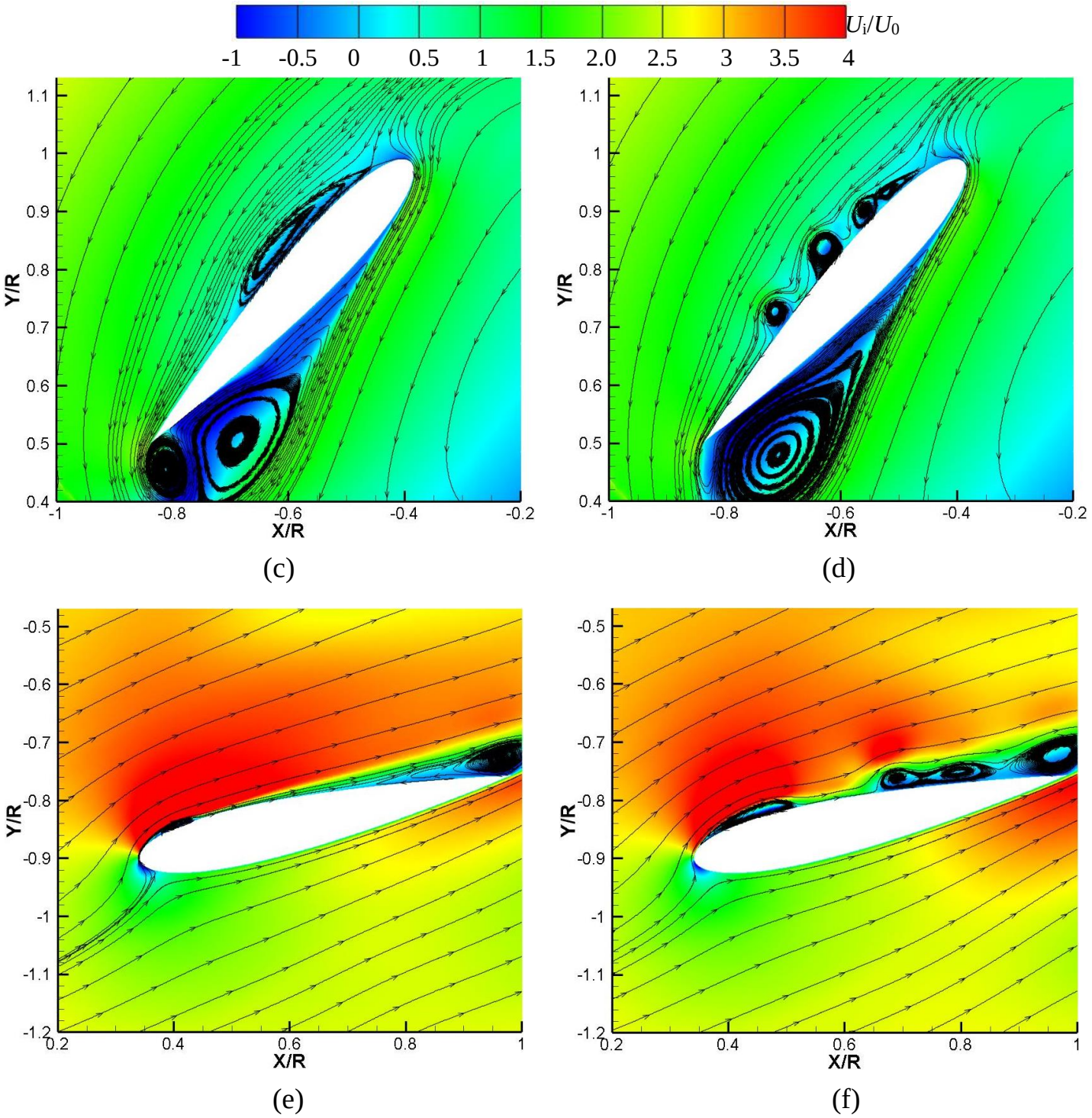

Fig.17 Pressure and relative velocity. (a) Pressure of blade A; (b) Pressure of blade B; (c) and (e) SST k-ω; (d) and (f) SST TM.

As shown in figure 18, the velocity and vorticity contours at λ=0.73 are displayed and the computational results are compared with the experimental data. At ψ=0º, the wake of blade A has no contact with blade B. But blade B has a visible interaction with the wake shedding from itself near the leading edge. Compared with that in figure 12, the interaction position is much closer to the leading edge, due to the change of the relative velocity U_{rel}. It also can be seen that the blade-wake

interaction predicted by SST *k-ω* is more obvious. The pressure, relative velocity and velocity profiles are shown in figure 19 to study the near-wall flows and its impact on the performance of the single blade. According to the simulation results, it is found that the pressure distribution of blade B on the suction side has relatively large difference. The large relative velocity develops from the leading edge to the trailing edge for SST TM, leading to the performance enhancement because of the lower pressure, as shown in figure 19b. This occurrence is due to the prediction of the low-pressure region near the leading edge and less impact of blade-wake interaction for SST TM in figure 18f. In addition, the pressure has the fluctuation for SST *k-ω* model, as a result of many individual vortices. Very close to the wall, the reverse flow occurs earlier for SST TM, for the reason that it has the ability to detect the instability of the boundary layer disturbed by the external environment. Moreover, near the leading edge of the pressure side, the external flow structure is strongly affected by the blade-wake interaction for SST *k-ω* model, which is shown in figure 19e and 19f.

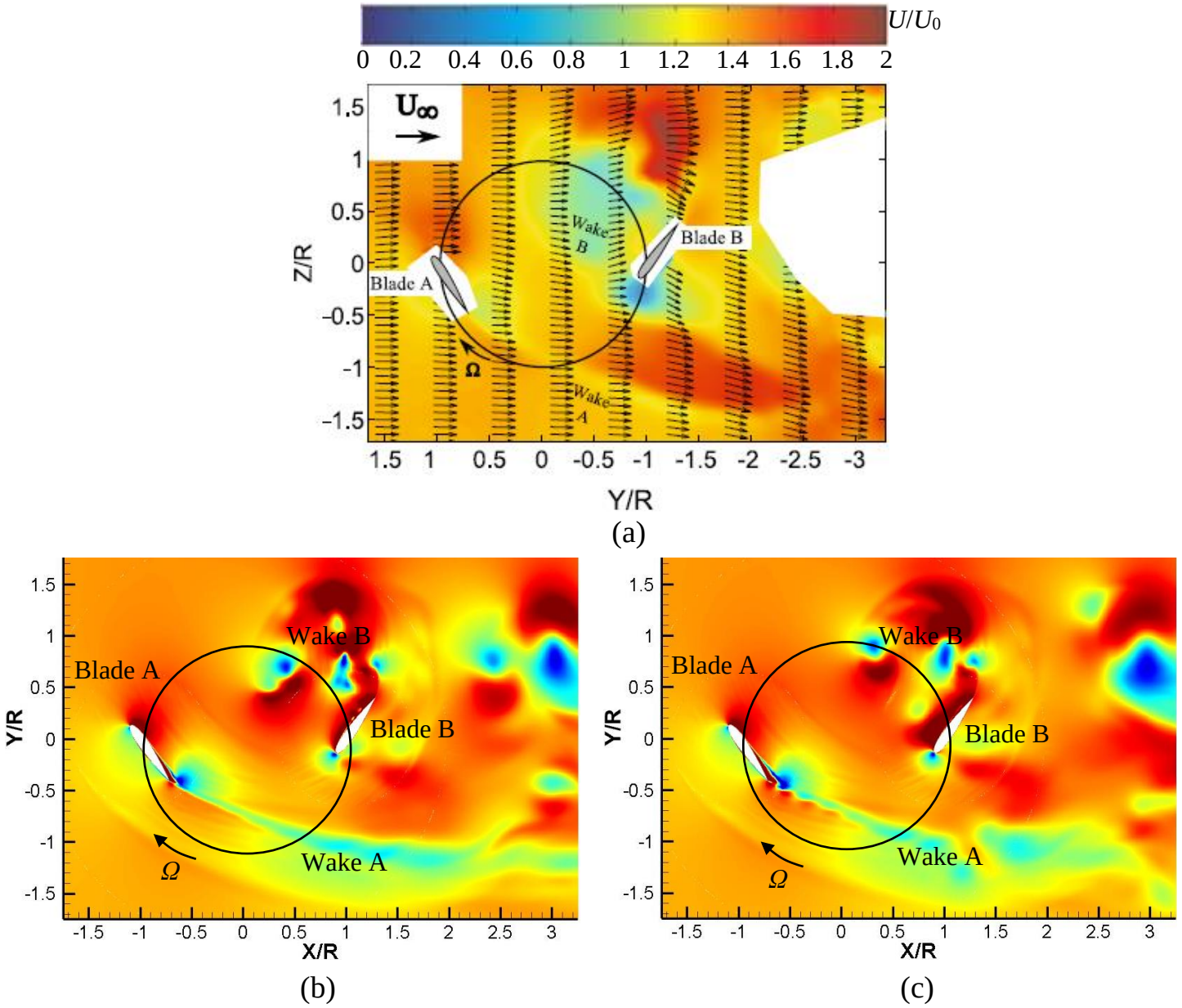

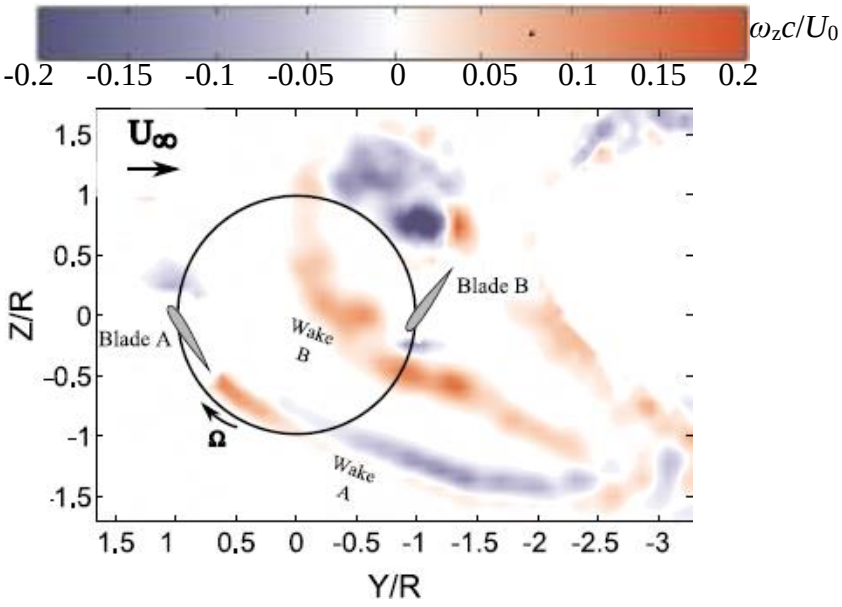

(d)

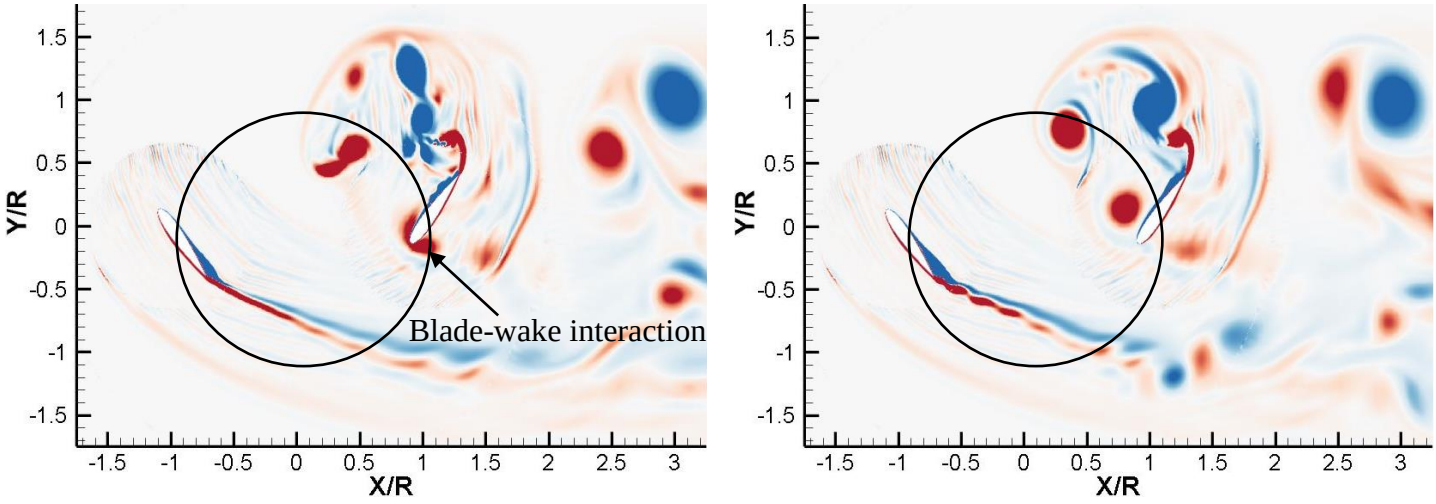

(e) (f)

Fig.18 Velocity and vorticity contours. (a) and (d) Experiments; (b) and (e) SST *k*-*ω*; (c) and (f) SST TM.

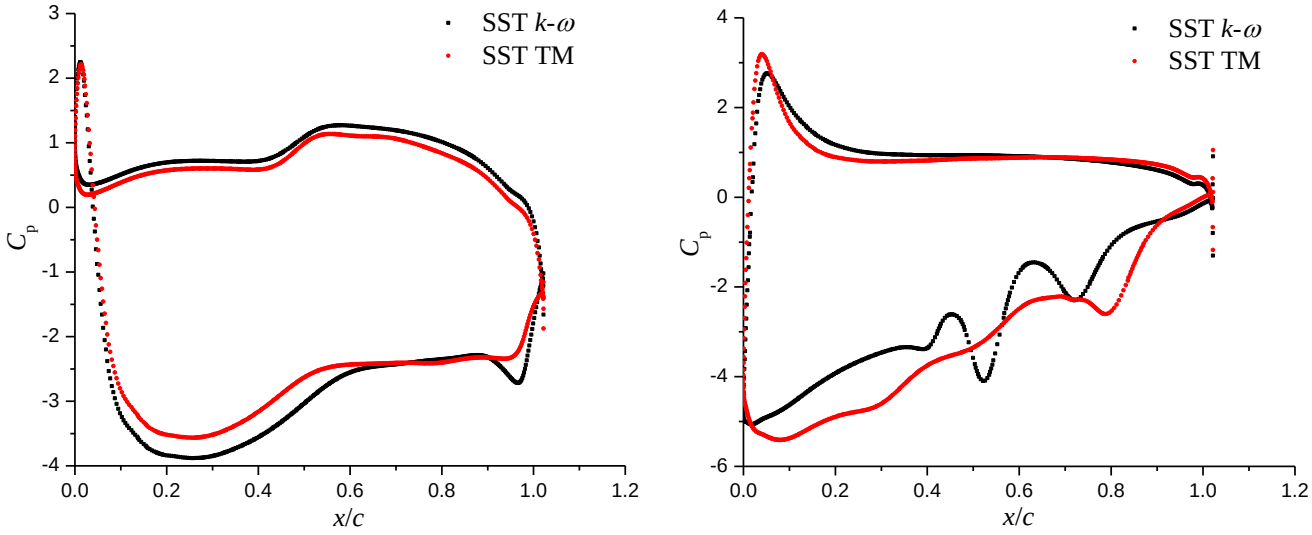

(a) (b)

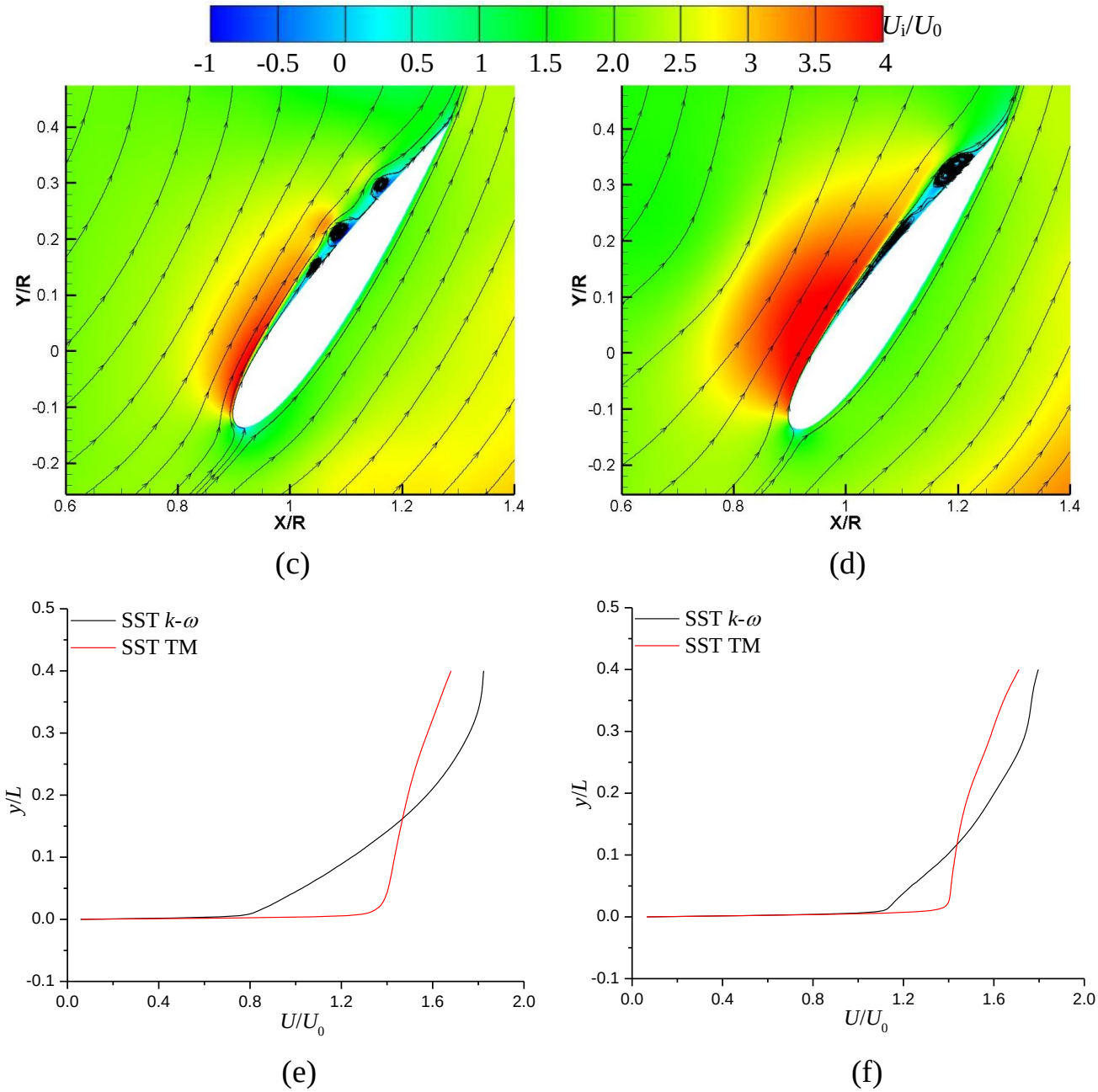

Fig.19 Pressure, relative velocity and velocity profiles. (a) Pressure of blade A; (b) Pressure of blade B; (c) SST k-ω; (d) SST TM; (e) Velocity profile of blade B at x/c=0.05 on pressure side; (f) Velocity profile of blade B at x/c=0.15 on pressure side.

At ψ=30°, the velocity and vorticity contours obtained by the simulations and experiments are shown in figure 20, when λ is 0.73. Although the flow structure is quite similar with that at λ=0.52, there is no blade-wake interaction at this position. The change of the relative velocity, due to the increase of the freestream velocity, modifies the trajectory of the wake shedding from blade A. But for blade B, the wake-wake interaction is still captured clearly by two turbulence models. To study the difference of flow structures near the blade surface, the blade loadings and velocity contours of two blades are shown in figure 21, respectively. The pressure distribution on the pressure side is quite similar for two turbulence models and a little difference

is induced by the existence of a small-scale attached vortex. Then, on the suction side of blade A, flow separation occupying a large part of the blade surface exists, particularly near the trailing edge, leading to the remarkable pressure difference. When it comes to the blade B, the turbulent boundary layer separation changes the blade loading evidently from the middle chord to the trailing edge, but this phenomenon becomes weak compared with that in figure 15. Ultimately, the results show that SST TM has the capability to capture more scales near the wall.

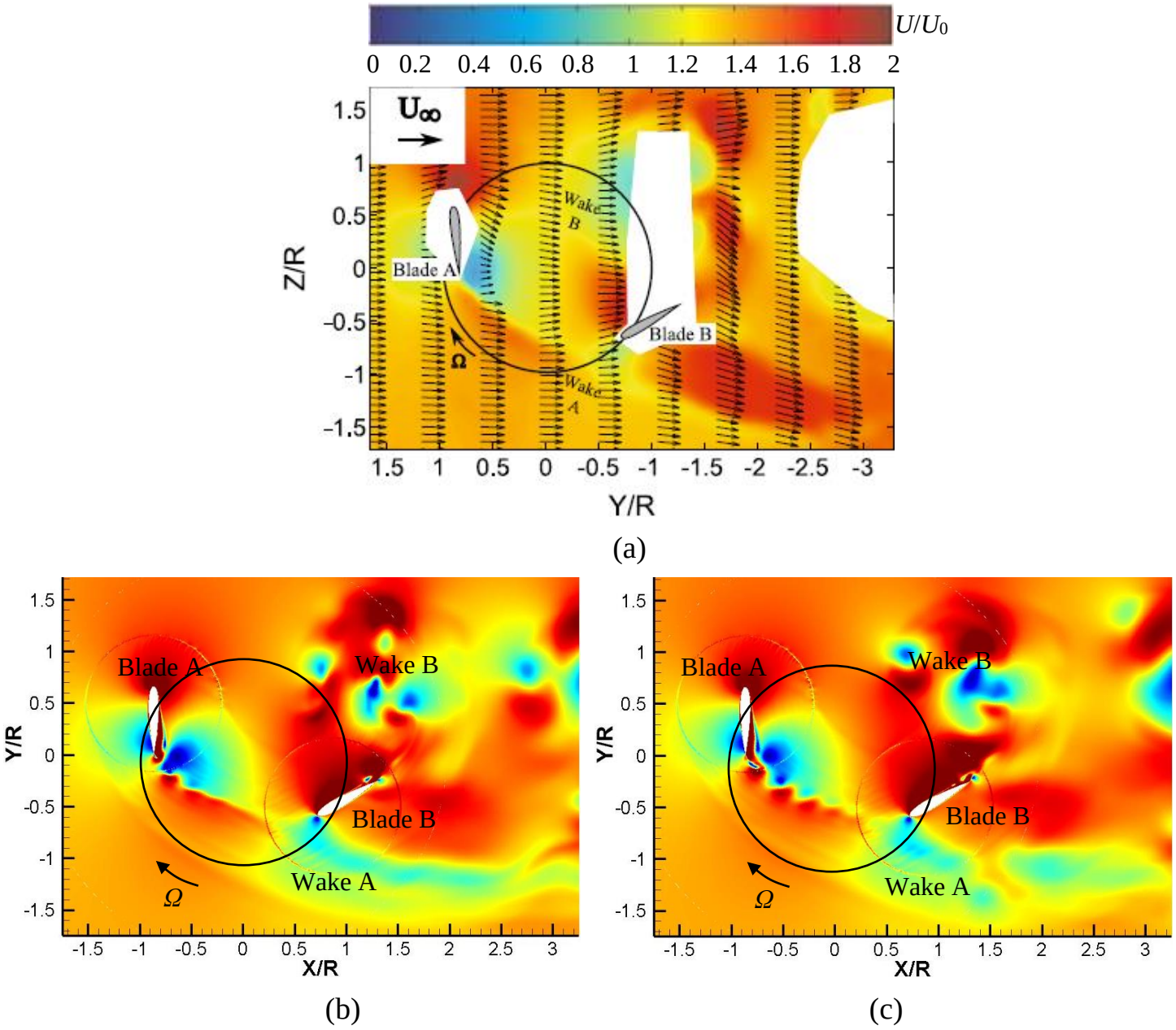

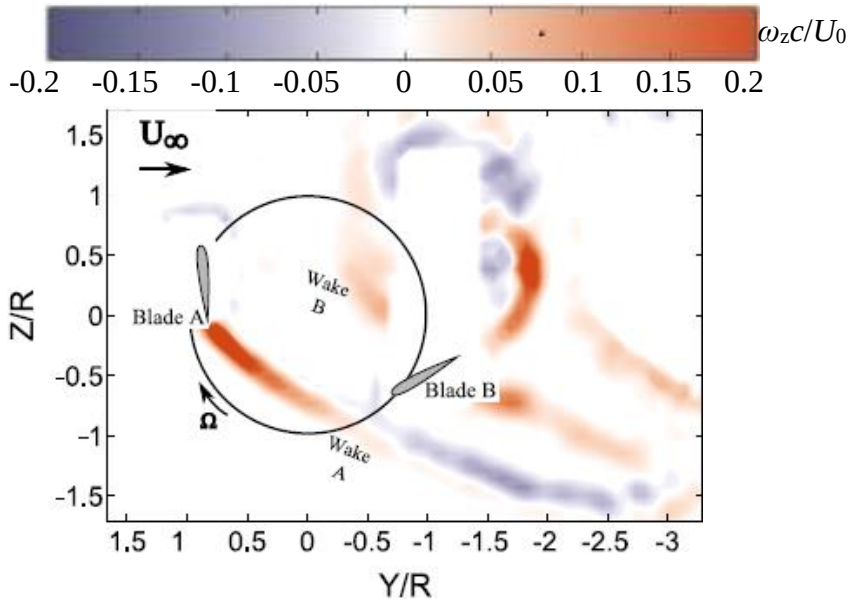

(d)

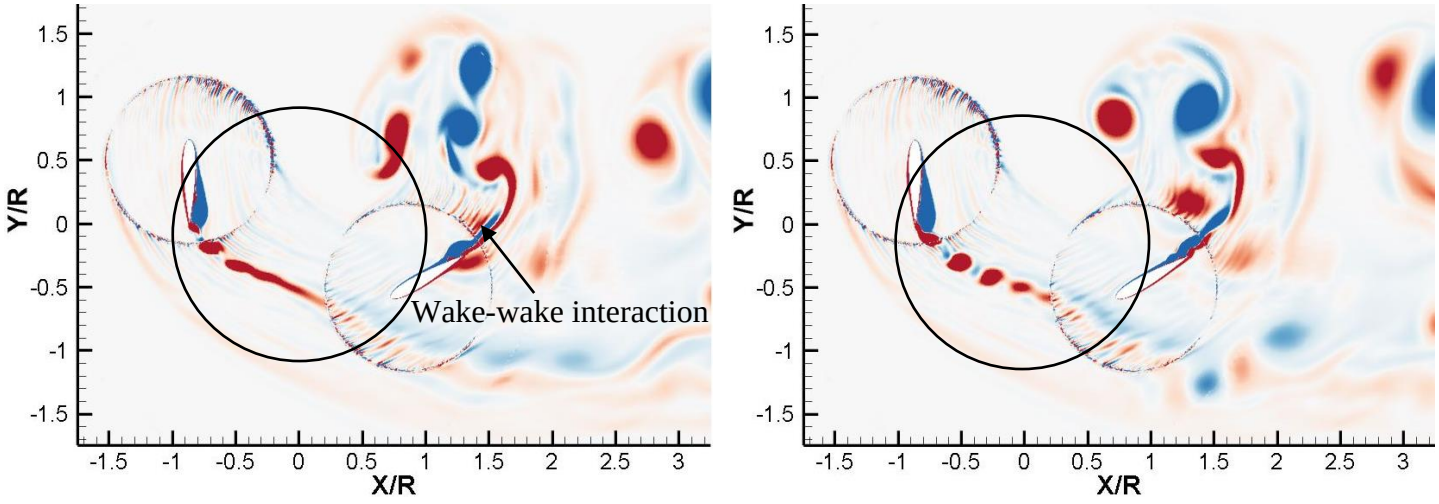

(e) (f)

Fig.20 Velocity and vorticity contours. (a) and (d) Experiments; (b) and (e) SST *k*-*ω*; (c) and (f) SST TM.

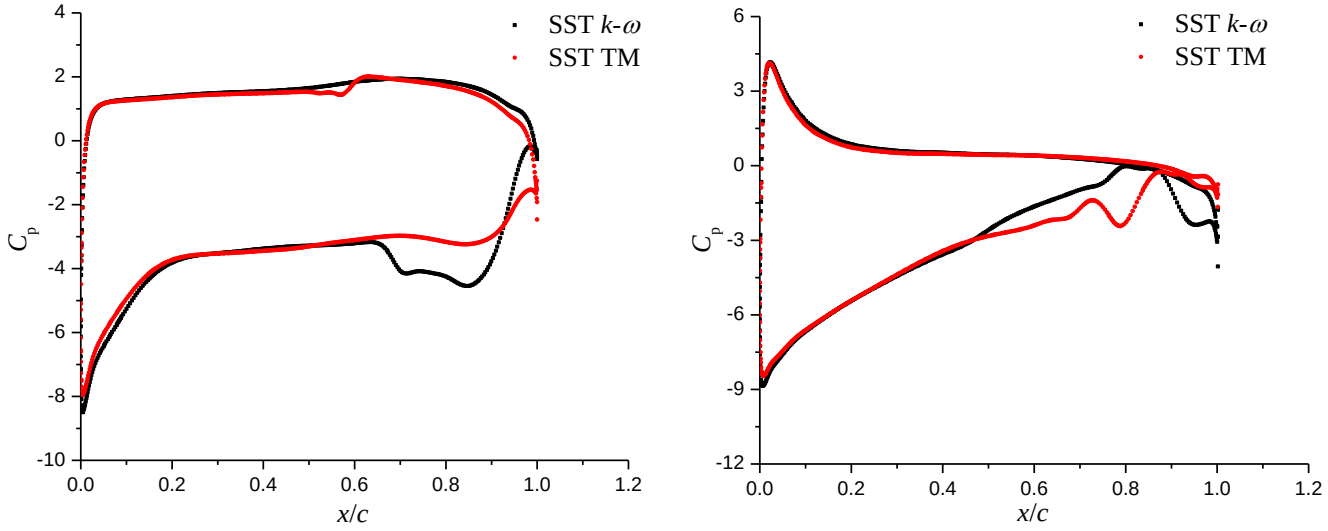

(a) (b)

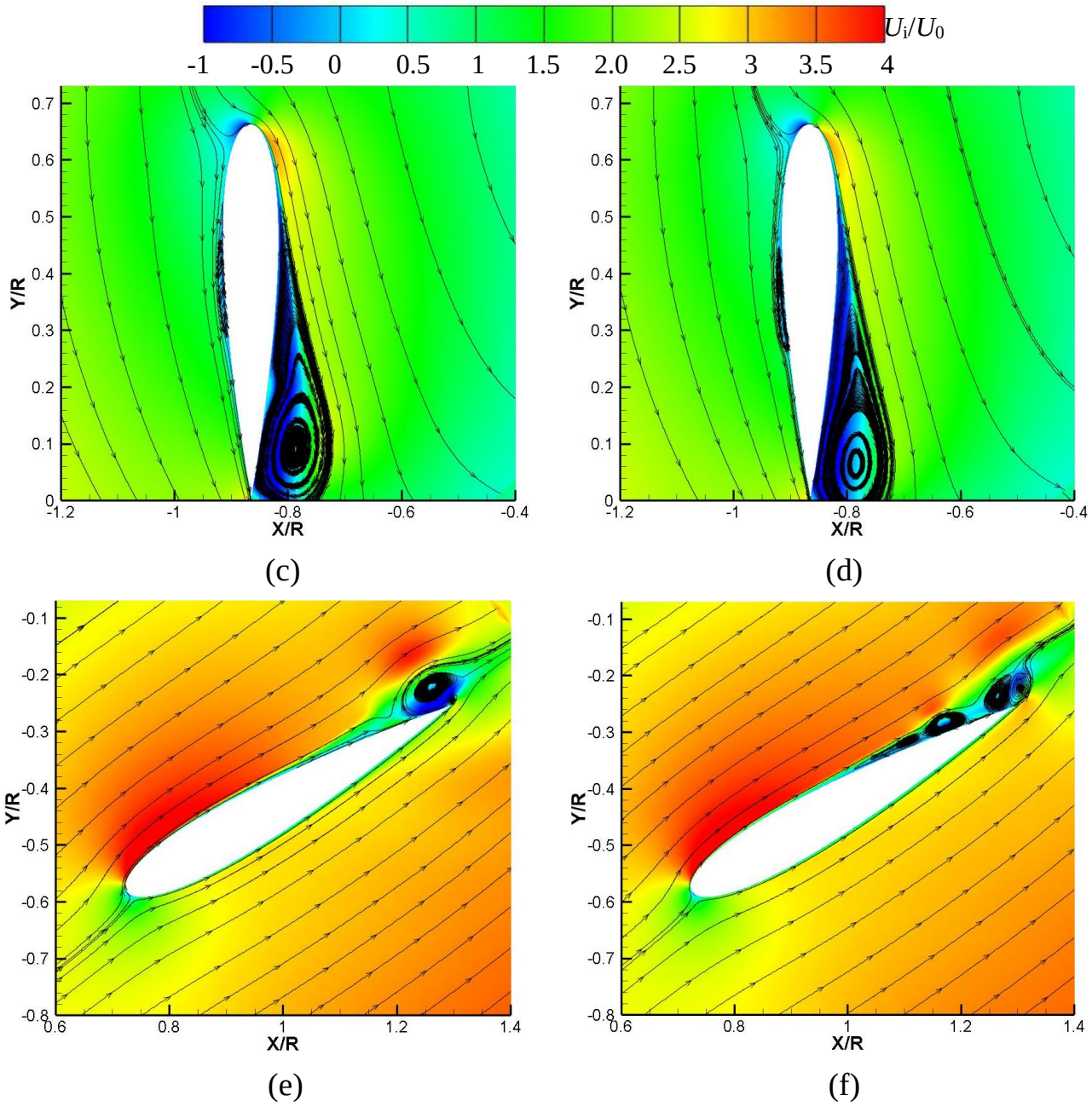

Fig.21 Pressure and relative velocity. (a) Pressure of blade A; (b) Pressure of blade B; (c) and (e) SST k-ω; (d) and (f) SST TM.

When ψ increases to 60°, the wake of blade A has a weak interaction with the wake B near the trailing edge, compared with that at λ=0.52. From the distributions of velocity and vorticity, it seems that the vortical flows obtained by SST TM are more unstable, characterized by more individual vortex in shedding wakes, as shown in figure 22e and 22f. As a complementary, the pressure and velocity contours are presented in figure 23, to analyze the detailed near-wall flow structures. For blade A, it is undergoing the retreating side and massive flow separation nearly exists on the whole suction side, particularly from x/c=0.4~1.0. There are three vortex structures located at the leading edge. After the reattachment, the turbulent boundary layer separates and two vortices connecting with each other are generated. Evidently, the

presence of the trailing edge flow separation causes a lower pressure for SST *k-ω* model, leading to a better performance for blade A. On the suction side of blade B, there is only a small vortex attached on the blade trailing edge for SST *k-ω* model, but SST TM captures the slender separation bubble, the reattachment and the turbulent boundary layer separation clearly.

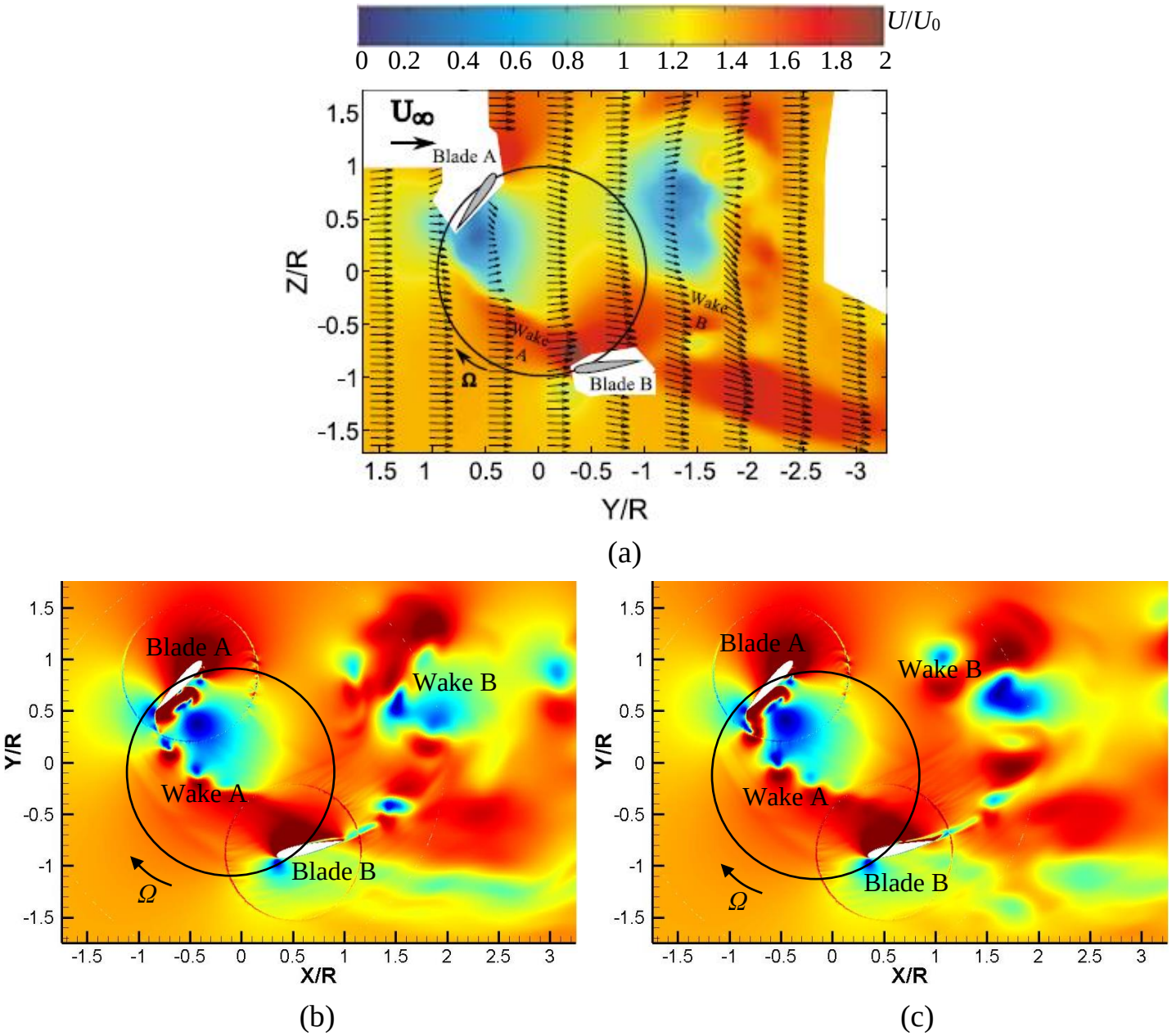

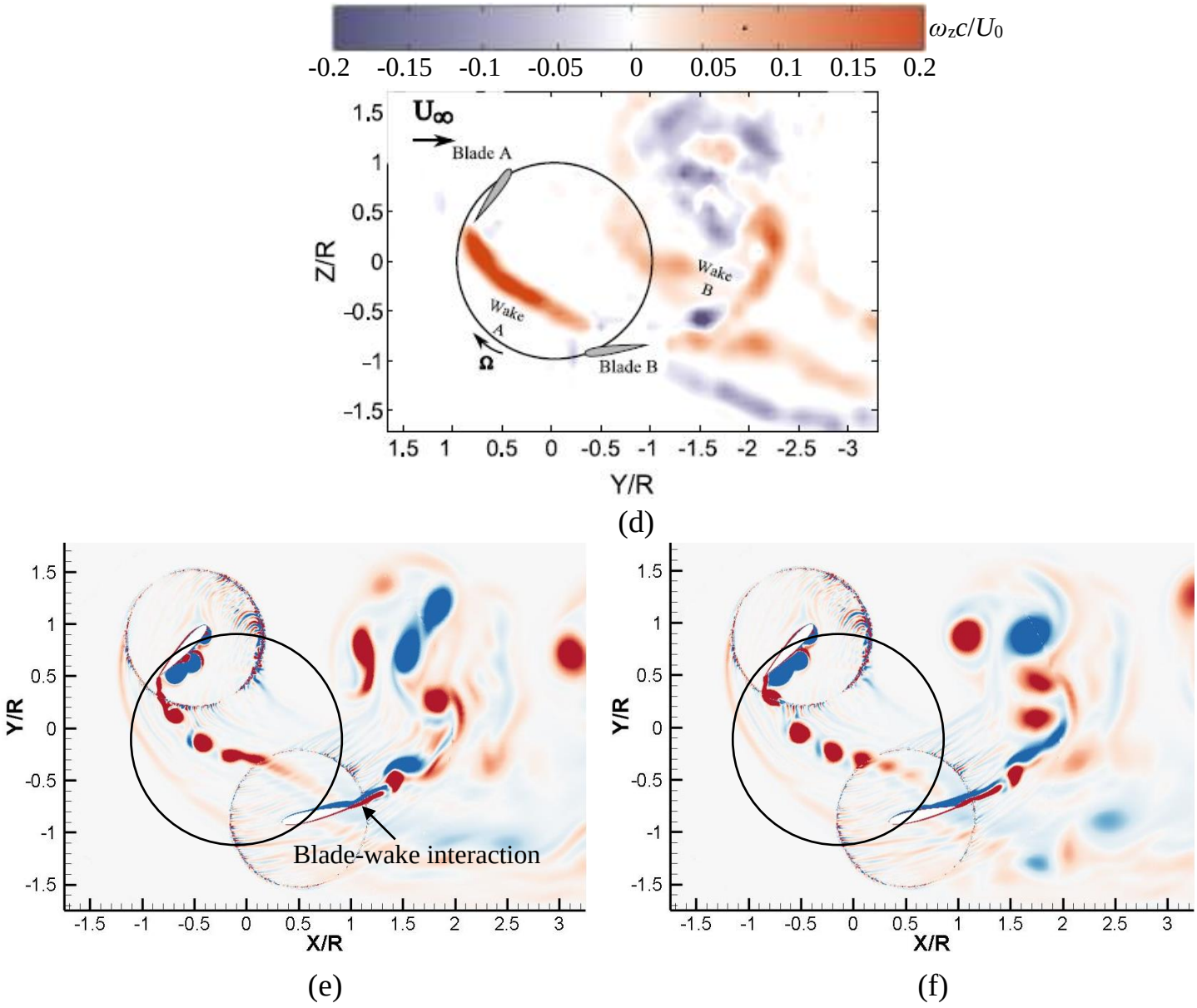

Fig.22 Velocity and vorticity contours. (a) and (d) Experiments; (b) and (e) SST *k*-*ω*; (c) and (f) SST TM.

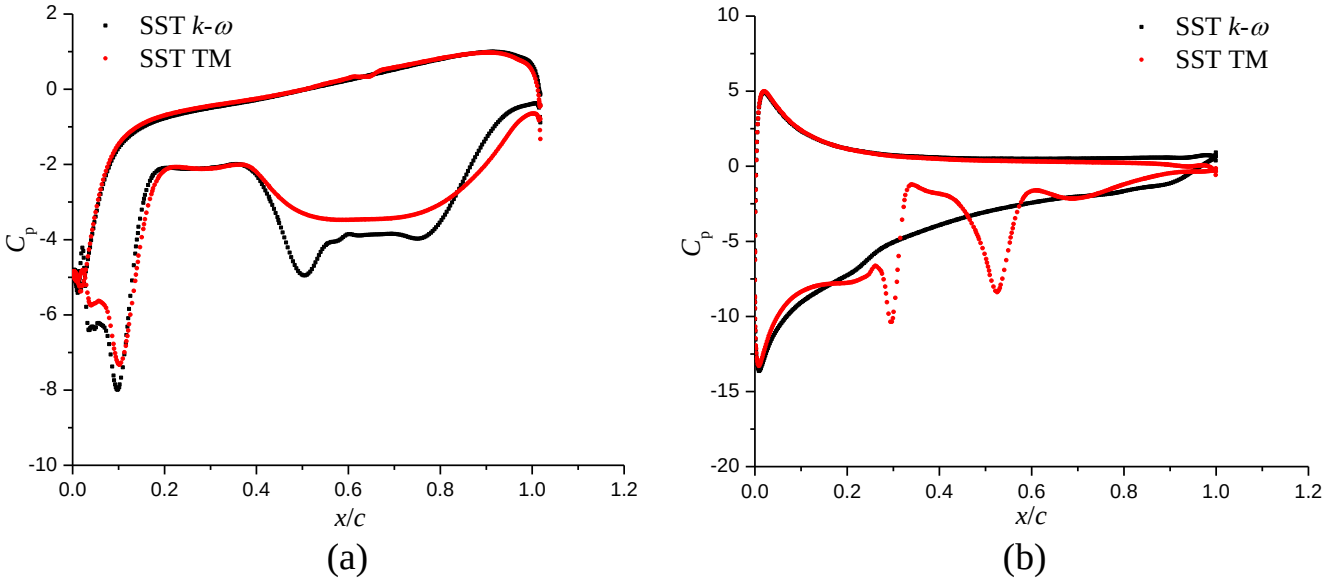

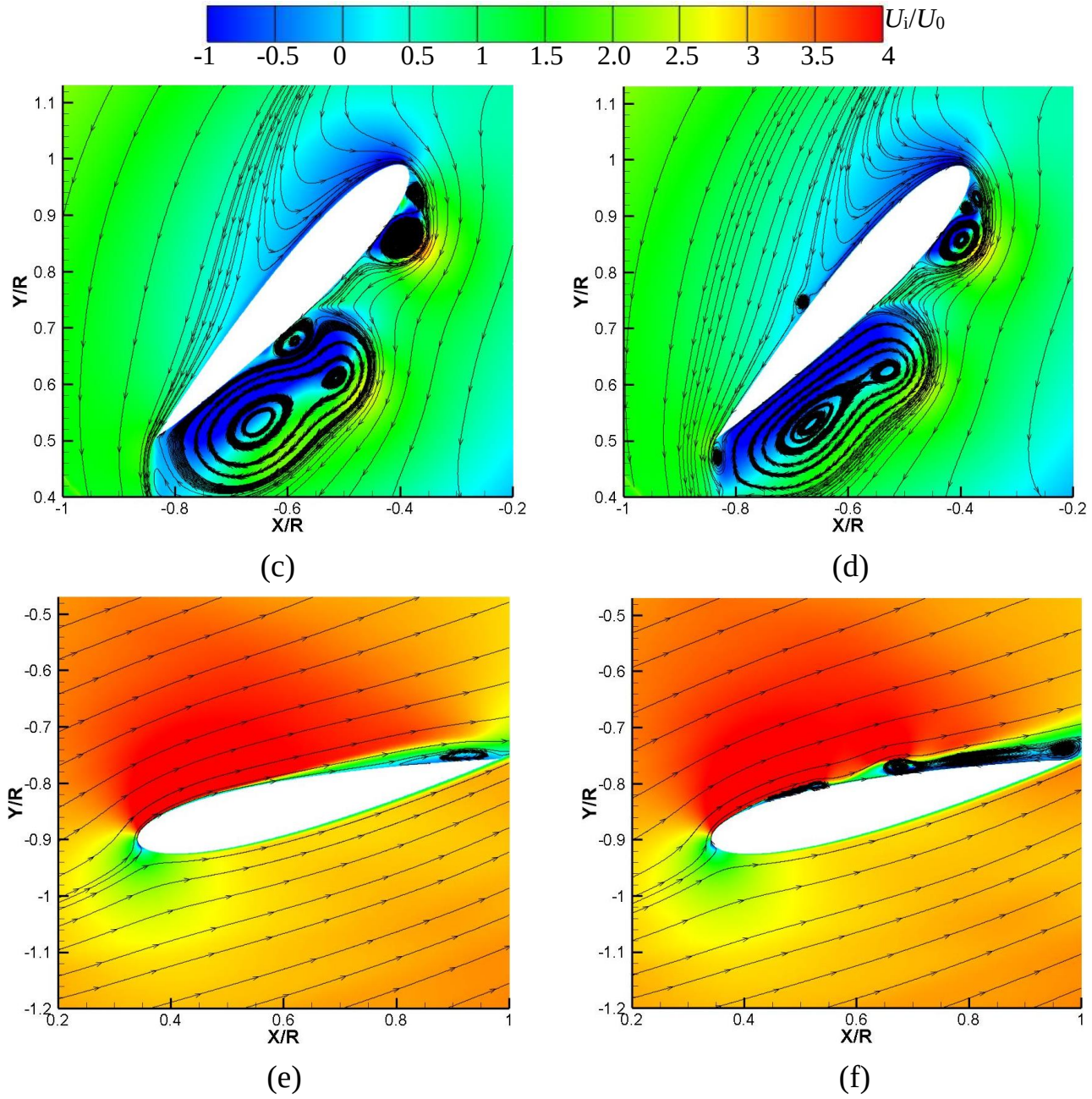

Fig.23 Pressure and relative velocity. (a) Pressure of blade A; (b) Pressure of blade B; (c) and (e) SST *k*-ω; (d) and (f) SST TM.

The global performance of the cycloidal rotor at two λ are displayed in figure 24, to explain the difference of lift and propulsive force coefficients predicted by two different turbulence models. It can be seen that the main difference of the lift coefficient is nearly at ψ=30° and 90° while it is at ψ=30° for the propulsive force difference when λ is 0.52. At ψ=30°, the blade A is almost vertical and the vertical force is almost equal to zero, which is shown in figure 10a. Due to the components of the lift and drag in Y axis, the large magnitude of the lift for the cycloidal system is provided by blade B. However, in figure 15b, the blade loading obtained by SST TM is larger than that of SST *k*-ω model because of the earlier and more intensive flow separation near the trailing edge, resulting in the larger lift of the cycloidal rotor.

Furthermore, blade B can provide the positive propulsive force, but its magnitude is larger for SST TM as a consequence of the larger blade loading in figure 15b. Simultaneously, blade A produces the negative propulsive force due to the components of the lift and drag in X axis, which is shown in figure 11a. As a result, according to the propulsive force generated by two blades, SST *k*-ω model achieves the negative propulsive force with large value.

Then, at ψ=90°, based on the force sketch in figure 11b and 11d, each blade can generate the vertical force completely provided by the lift, but with different values shown in figure 25a and 25b. Obviously, the vertical force on blade B is much larger than blade A, which brings about the positive lift of the cycloidal rotor. For blade A, the pressure difference predicted by two turbulence models is due to the large flow separation on the trailing edge of the suction side. However, the impact is more apparent for SST *k*-ω model. In addition, on the pressure side, the flow state is also extremely different, as presented in 25c and 25d. Blade B also makes the contribution to the lift difference of the rotating system, and the blade loading obtained by SST TM is much larger than SST *k*-ω model, resulting from the attached large-scale laminar separation bubble. Generally, it concludes that the massive flow separation on the suction side of blade A has greater impact on the blade loading for SST *k*-ω model, while the laminar separation bubble with large size predicted by SST TM is the main contributor to the large pressure difference of blade B.

As λ increases to 0.73, the noticeable phenomenon is the negative propulsive force with large magnitude at ψ=30°, compared with that at λ=0.52. By the comparison of pressure distributions in figure 15a and 21a, there is no much difference for blade A, which means that the negative propulsive force created by blade A is quite similar with the increase of λ. However, for blade B, the positive propulsive force at λ=0.52 is much larger than that at λ=0.73, because of the larger blade loading shown in figure 15b, compared with that in figure 21b.

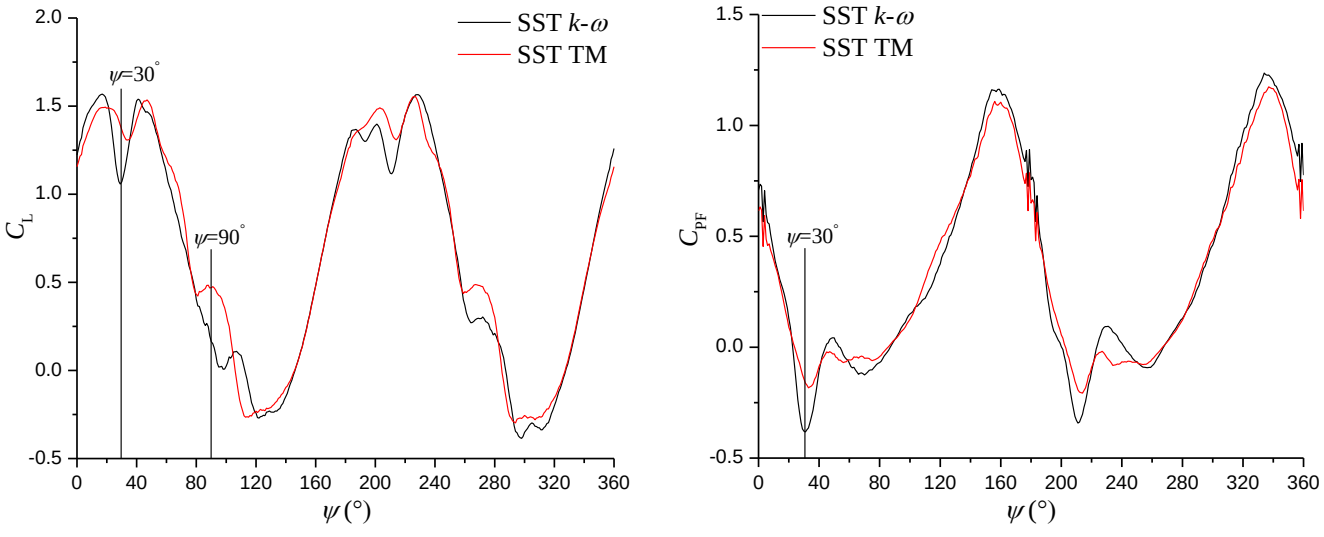

(a) (b)

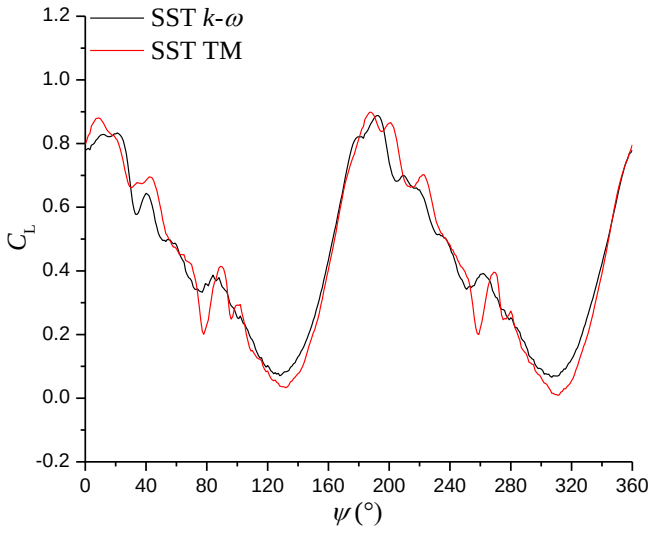

(c)

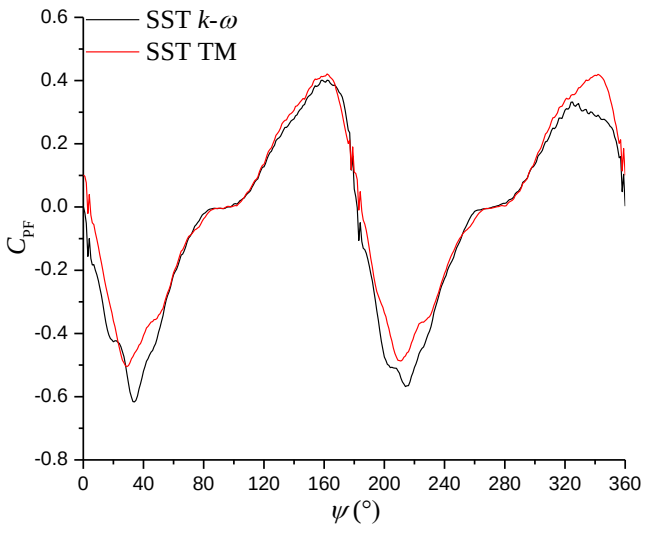

(d)

Fig.24 Instantaneous performance of the rotating system. (a) and (b) Lift and propulsive force coefficients at λ=0.52; (c) and (d) Lift and propulsive force coefficients at λ=0.73.

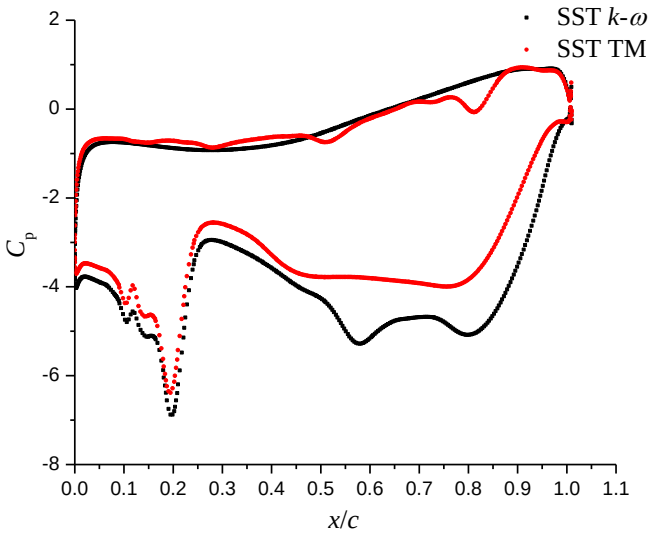

(a)

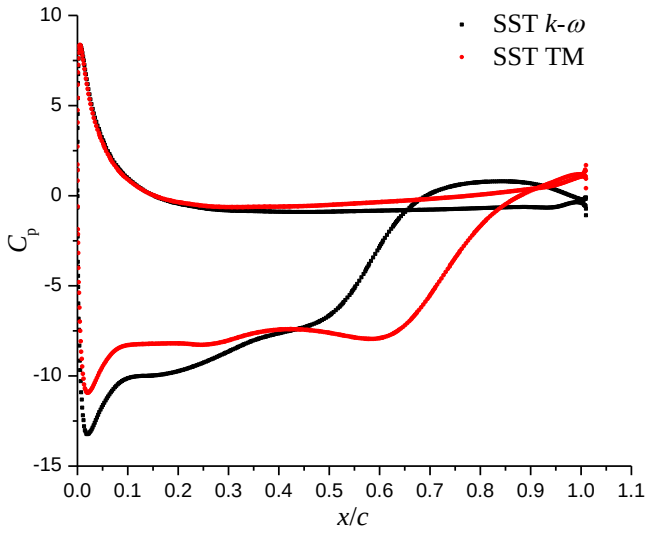

(b)

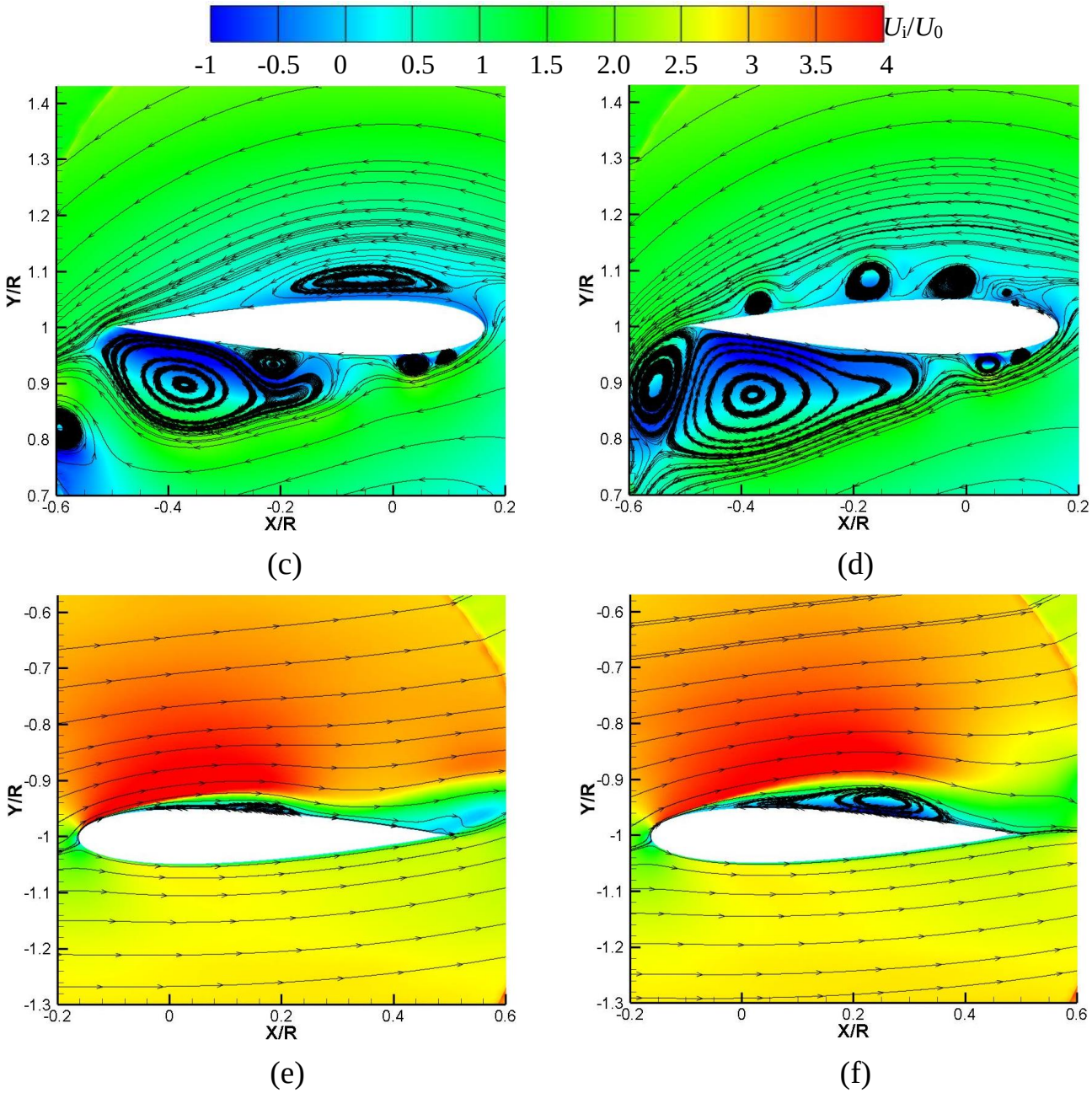

Fig.25 Pressure and relative velocity. (a) Pressure of blade A; (b) Pressure of blade B; (c) and (e) SST k-ω; (d) and (f) SST TM.

4.2 Main features of laminar-turbulence transition

In this section, the characteristics of laminar-turbulence transition over the blade surface at two λ for SST k-ω model and SST TM are discussed thoroughly. Several positions at advancing side are selected to clarify the transition evolution. The distributions of turbulent kinetic energy at λ=0.52 and the corresponding skin friction coefficients ($C_f=\tau_w/(0.5*\rho*U_0^2)$, where τ_w is wall shear stress) are displayed in figure 26 and 27, respectively. In this work, it is found that both two turbulence models can capture the existence of the separation bubble (SB) leading to the transition near the leading edge, due to the extremely low Reynolds number. By using

SST TM, Winslow et al. [32] pointed out that there is a large-scale leading-edge flow separation bubble, when the Reynolds number is below 5×10^4, which is quite similar with the event in the current investigation. For the SST k-ω model, the relatively small separation bubble is observed while SST TM can capture the SB with a relatively large size. Additionally, it seems that the separation bubble obtained by SST TM is composed of multiple vortices initially. Dong et al. [33] observed that a nonclassical laminar separation bubble structure, which includes two vortices with the cores locating around the transition point, is evident with the increase of Reynolds number to 5×10^5. On the oscillating airfoil, Negi et al. [34] used the large eddy simulation to investigate the transition over a pitching airfoil with a small amplitude, and the main results reveal that there is spatially growing wave of the laminar boundary layer when the LSB is absent. These growing waves are amplified gradually with the increases of LSB size, which indicates that the transition is triggered by this laminar boundary layer instability. Usually, after the reattachment, the boundary layer would become fully turbulent until the occurrence of the turbulent boundary layer separation, which is often detected over the stationary objectives. However, in figure 26b, the boundary layer is still laminar after the reattachment, which is presumably ascribed to the laminar flow occupying large portion of the upper surface at low Reynolds number and the delayed transition resulting from the dynamic effect [35]. Conversely, the flow after the SB is fully turbulent for SST k-ω model. Then, at ψ=60°, the separation bubble has already formed and it expands towards the middle chord and the separated flow near the trailing edge sheds into the wake gradually. In general, the bubble size obtained by SST TM is relatively larger and the development of the transition is predicted more clearly. From the distributions of skin friction coefficients in figure 27, it is evident that the flow separation is always near the leading edge and the reattachment point moves downstream with the increase of ψ, which is because the transition is normally located at the trailing edge when the relative attack-of-angle is small. Additionally, it is discovered that there is no difference in flow separation point for two turbulence models, but the transition and reattachment locations are more upstream for SST k-ω model, as a consequence of the separation bubble size.

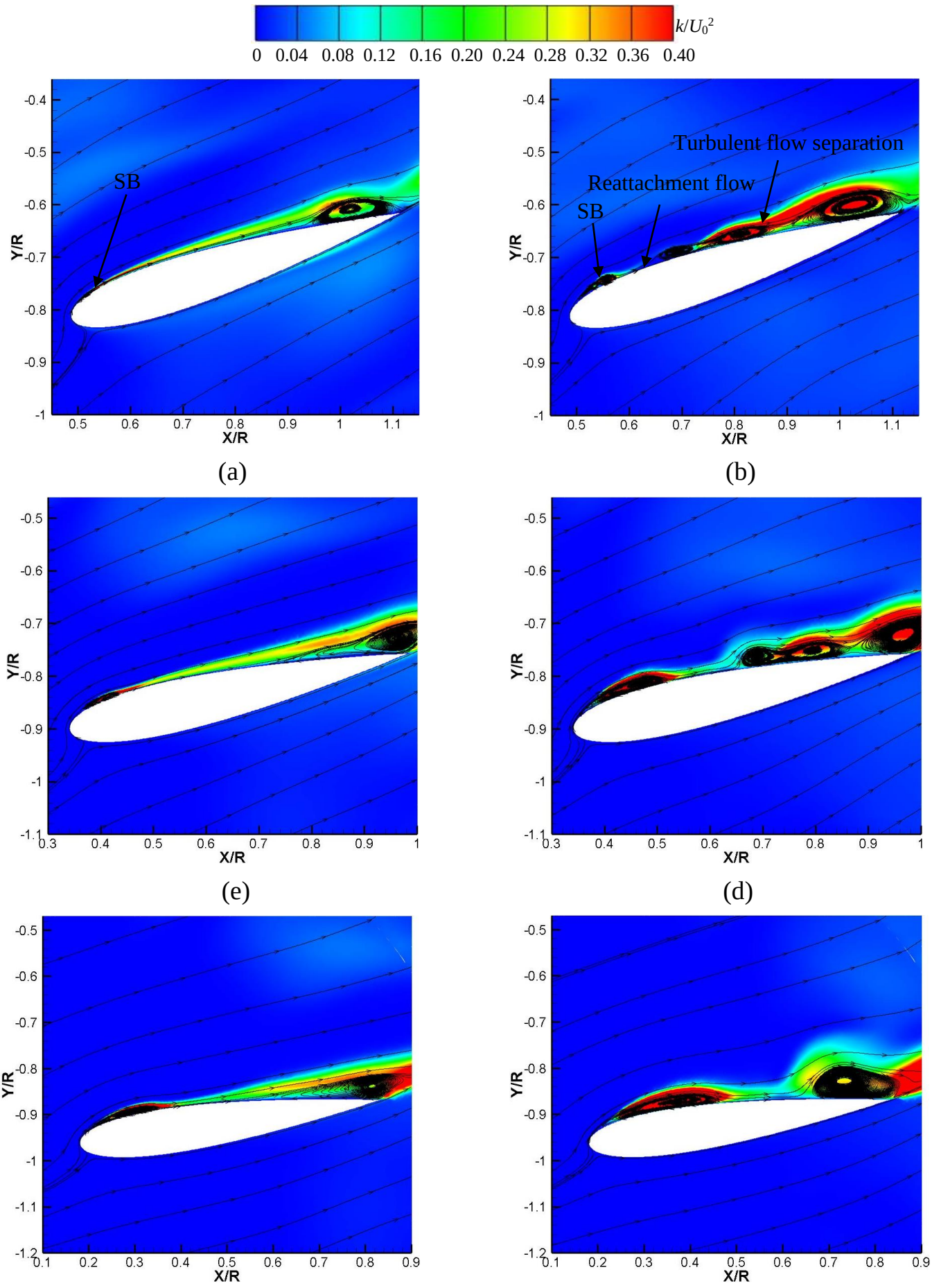
k/U_0^2
0 0.04 0.08 0.12 0.16 0.20 0.24 0.28 0.32 0.36 0.40
SB
Turbulent flow separation
Reattachment flow
SB
Y/R
X/R
(a)
(b)
(e)
(d)
(e)
(f)

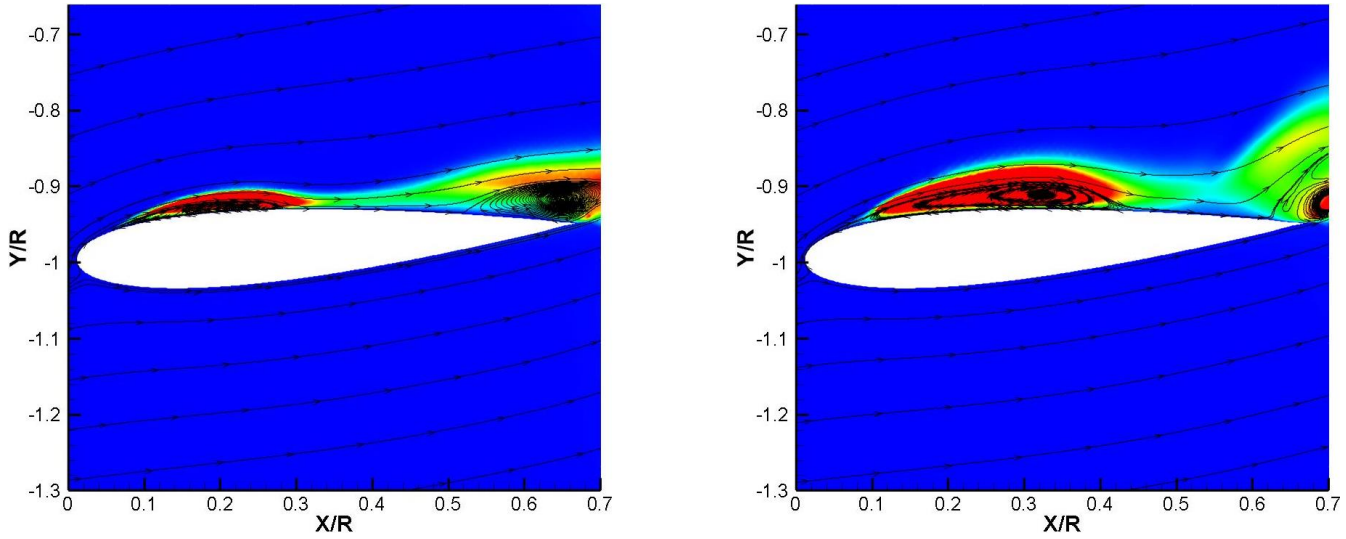

(g) (h)

Fig.26 Distributions of turbulent kinetic energy (Left column is SST k-ω model while right column is SST TM). (a) and (b) ψ=50°; (c) and (d) ψ=60°; (e) and (f) ψ=70°; (g) and (f) ψ=80°.

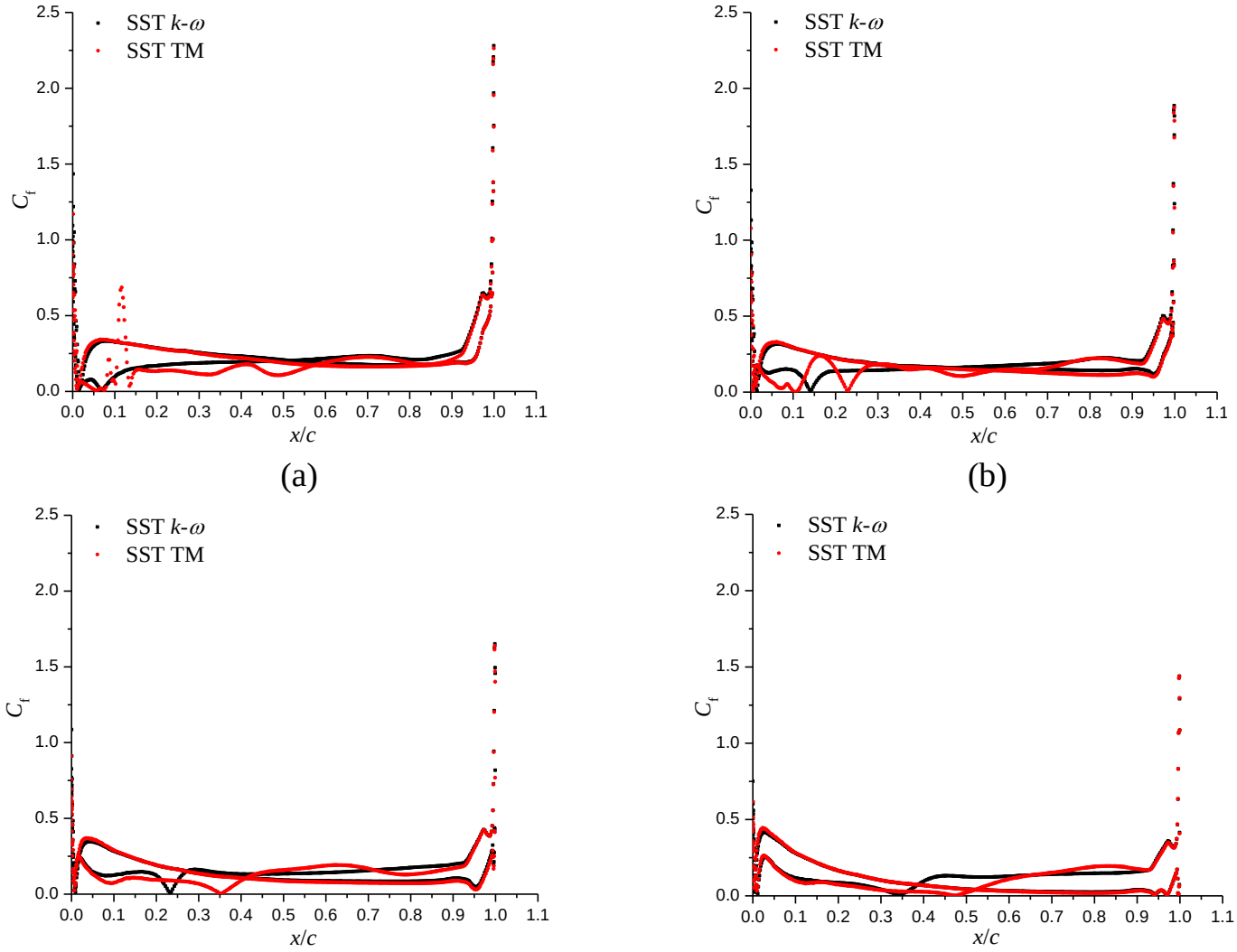

(a) (b)

(c) (d)

Fig.27 Distributions of skin friction coefficients at different ψ. (a) ψ=50°; (b) ψ=60°; (c) ψ=70°; (d) ψ=80°.

Afterwards, the distributions of turbulent kinetic energy and skin friction coefficients at λ=0.73 are shown in figure 28 and 29, respectively. In figure 28b, the roll-up vortices cause the growing wave of the laminar boundary layer when the separation bubble does not occur. Obviously, the shape of roll-up vortices is much slenderer than that at λ=0.52, due to the change of the relative velocity. When the flow separation appears near the trailing edge, the level of the turbulent kinetic energy becomes very high. However, for SST k-ω model, the fully turbulent boundary layer is observed after the separation bubble with a small size, which means that the formation of the separation bubble is delayed as the Reynolds number increases. At next moment, as shown in figure 28c, the separation bubble gradually develops and it moves towards the middle chord gradually as the relative attack-of-angle becomes smaller. Then, in figure 28f, the region where two vortices co-exist has high level of turbulent kinetic energy, leading to the local transition onset. Downstream from the reattachment point, the boundary layer is still laminar and a vortex is evident, leading to a small change of the skin friction coefficient shown in figure 29c. Finally, at the incidence where the relative velocity coincides with the airfoil leading edge, a separation bubble is totally formed by two vortices and the vortex after the reattachment of the separation bubble is located near the trailing edge. Generally, it concludes that the roll-up vortices lead to the growing wave of the laminar boundary layer and then the local transition onset is induced by two distinctive vortices. Consequently, the single separation bubble is generated by these two vortices and it develops towards the trailing edge. In figure 29, it is observed that the roll-up vortices cause the jump of the wall shear stress. Increasing the freestream velocity leads to the flow separation, transition and reattachment points moving downstream, especially for the reattachment point.

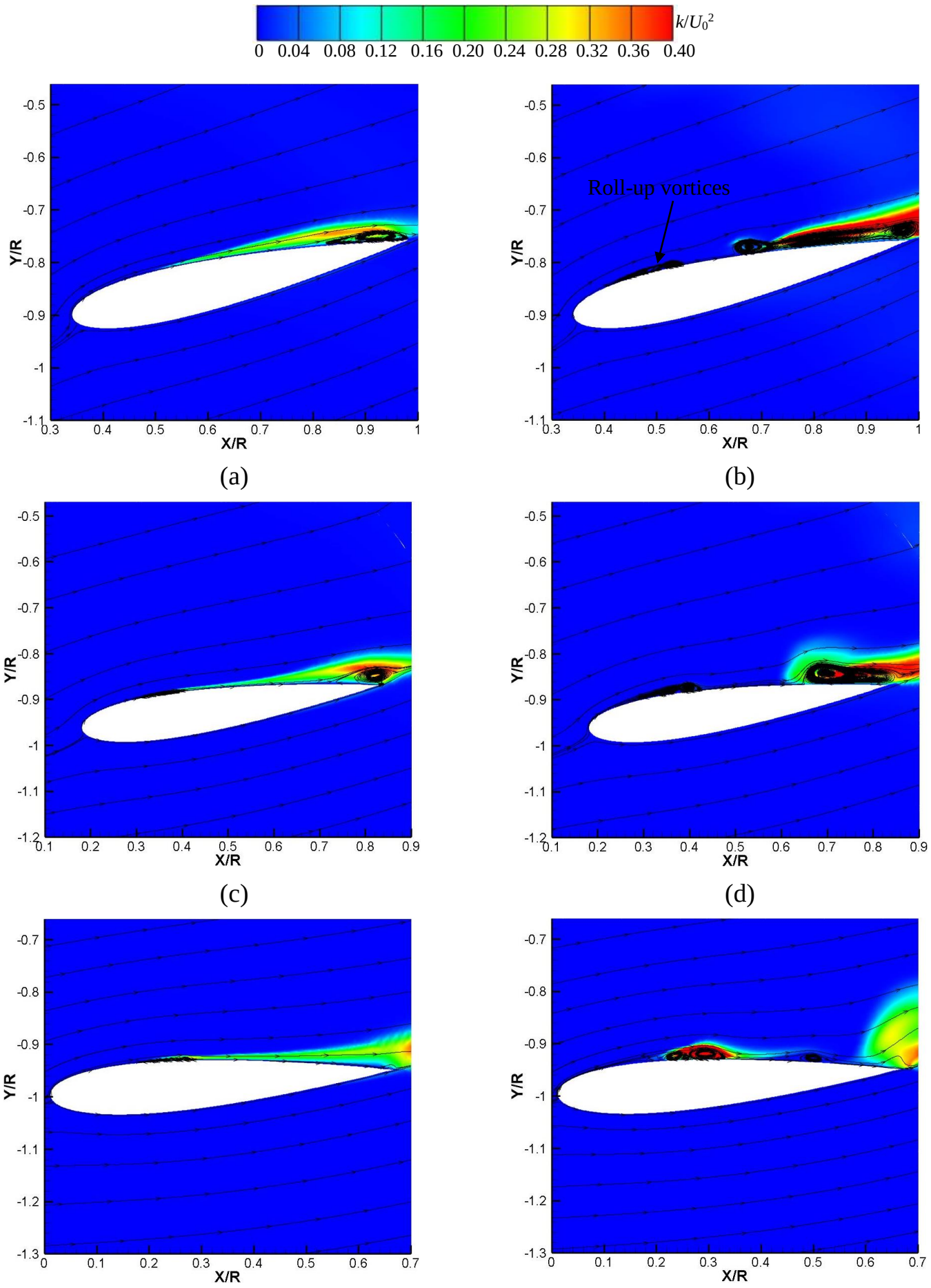
k/U_0^2
0 0.04 0.08 0.12 0.16 0.20 0.24 0.28 0.32 0.36 0.40
Roll-up vortices
Y/R
X/R
(a)
(b)
(c)
(d)
(e)
(f)

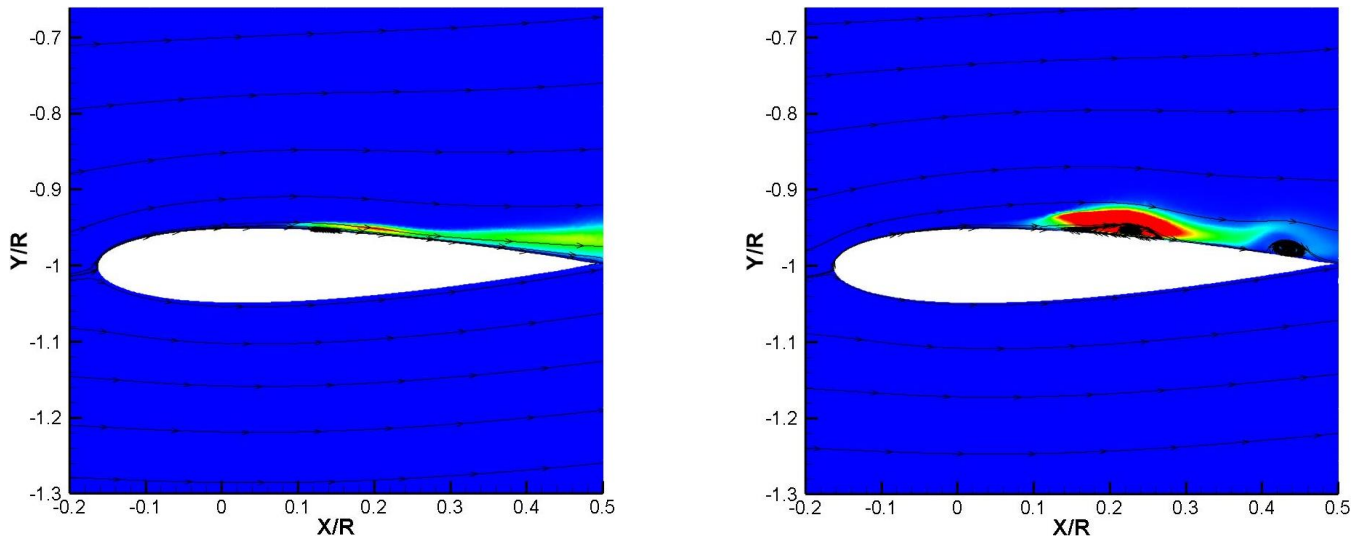

(g) (h)

Fig.28 Distributions of turbulent kinetic energy (Left column is SST k-ω model while right column is SST TM). (a) and (b) ψ=60°; (c) and (d) ψ=70°; (e) and (f) ψ=80°; (g) and (f) ψ=90°.

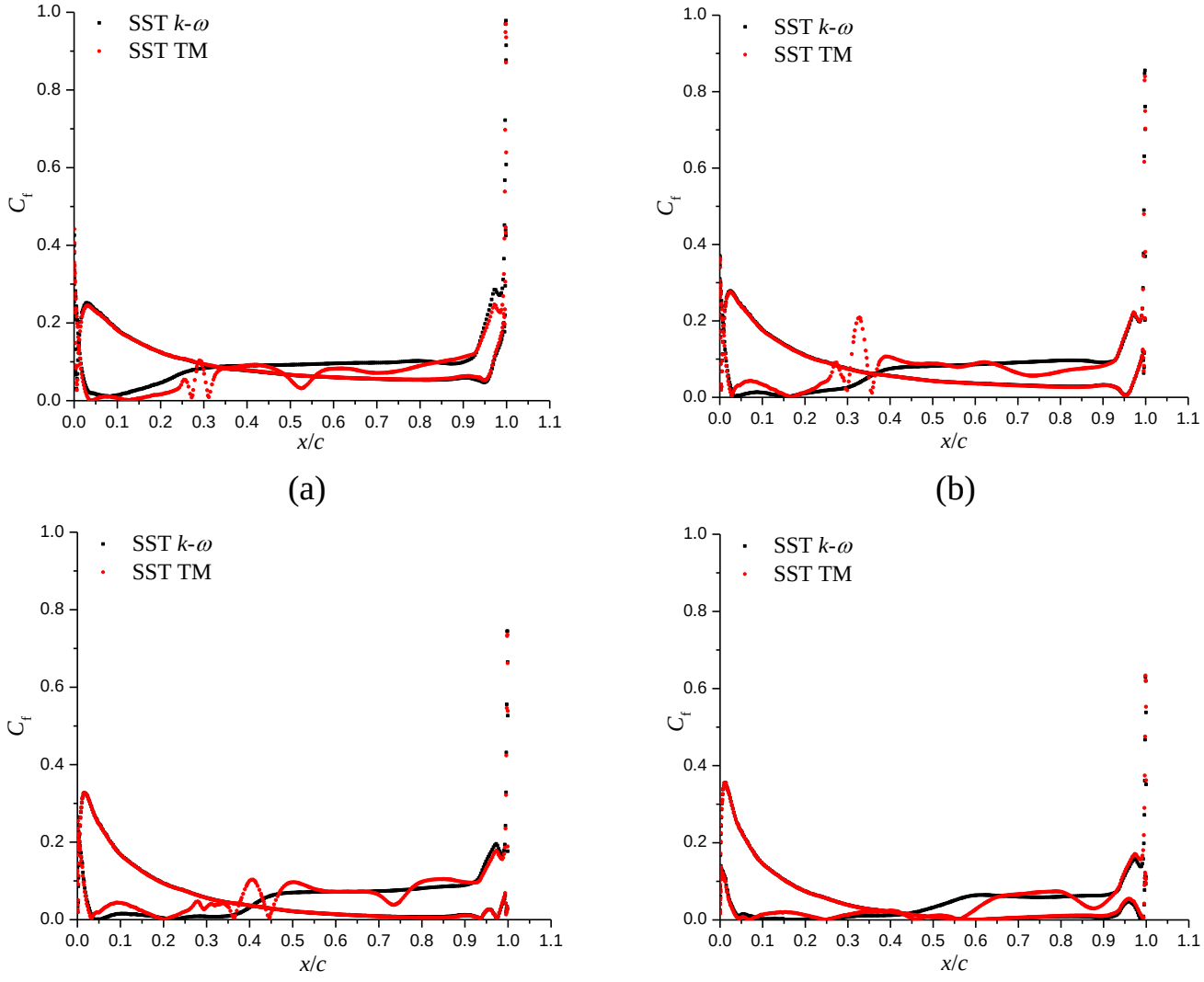

(a) (b)

(c) (d)

Fig.29 Distributions of skin friction coefficients at different ψ. (a) ψ=60°; (b) ψ=70°; (c) ψ=80°; (d) ψ=90°.

5. Concluding remarks

The unsteady vortical flows and laminar-turbulence transition over a 2-bladed cycloidal rotor is investigated using the original SST k-ω model and SST γ-$Re_{\theta t}$ transition model. The obtained results are compared with the available numerical and experimental data. The main conclusions are listed as follows:

(1) Among different turbulence models, the SST TM has the superiority in predicting the global performance of the cycloidal rotor, and the results obtained by RSM have large fluctuations due to the very refined mesh and small timestep.

(2) The transition of the vertical force, propulsive force and power from a negative/positive value to a positive/negative one, is analyzed using the force distribution on a single blade, which shows that increasing/decreasing λ has no impact on that. The transition of the vertical force is mainly at ψ=32° and 144°, where the blade profile is almost perpendicular to the horizontal axis, due to the balanced components of the lift and drag in the vertical direction. Moreover, the propulsive force transition occurs at ψ=90° and 270° when the blade geometry is parallel to the horizontal axis, due to the small value of the drag.

(3) Near the airfoil surface, the low-pressure and high-pressure zones near the blade leading edge due to the stagnation point deviation, the existence of the attached vortex, the massive flow separation and laminar-turbulence transition induced by the separation bubble, have a great impact on the performance of the cycloidal rotor system and single blade. In addition, the blade-wake and wake-wake interactions has a strong effect on the external flow filed.

(4) The main difference of the lift is at ψ=30° and 90° while it exists at ψ=30° for the propulsive force difference, due to the force direction and blade loading on the single blade. When analyzing the performance difference of the cycloidal rotor under different conditions, the force (vertical and propulsive forces) distribution of the single blade, the forces (lift and drag) acting on the blade and the pressure difference of each blade are necessary.

(5) The transition induced by the separation bubble at two λ when the blade undergoes the advancing side are revealed. It concludes that SST TM is highly sensitive to the disturbances and has the capability to capture the evolution of the transition, from the growing wave of the laminar boundary layer to the fully development of the separation bubble. However, the SST k-ω model only resolves the turbulent flow after the formation of the turbulent separation bubble.

Acknowledgement

The authors would like to show gratitude to China Scholarship Council (CSC) for the financial support. We also thank to Virginia Polytechnic Institute and State University to provide the computational platform.

Author declarations

The authors have no conflicts to disclose.

Data availability

The data that support the findings of this study are available from the corresponding author upon reasonable request.

References

[1] Lind, A. H., & Jones, A. R. (2016). Unsteady aerodynamics of reverse flow dynamic stall on an oscillating blade section. *Physics of Fluids*, *28*(7), 077102 (1-22).
[2] Koca, K., Genç, M. S., Açıkel, H. H., Çağdaş, M., & Bodur, T. M. (2018). Identification of flow phenomena over NACA 4412 wind turbine airfoil at low Reynolds numbers and role of laminar separation bubble on flow evolution. *Energy*, *144*, 750-764.
[3] Xu, J., Fu, Z., Bai, J., Zhang, Y., Duan, Z., & Zhang, Y. (2018). Study of boundary layer transition on supercritical natural laminar flow wing at high Reynolds number through wind tunnel experiment. *Aerospace Science and Technology*, *80*, 221-231.
[4] Simoni, D., Lengani, D., Ubaldi, M., Zunino, P., & Dellacasagrande, M. (2017). Inspection of the dynamic properties of laminar separation bubbles: free-stream turbulence intensity effects for different Reynolds numbers. *Experiments in Fluids*, *58*(6), 1-14.
[5] Ducoin, A., Loiseau, J. C., & Robinet, J. C. (2016). Numerical investigation of the interaction between laminar to turbulent transition and the wake of an airfoil. *European Journal of Mechanics-B/Fluids*, *57*, 231-248.
[6] Istvan, M. S., & Yarusevych, S. (2018). Effects of free-stream turbulence intensity on transition in a laminar separation bubble formed over an airfoil. *Experiments in Fluids*, *59*(3), 1-21.
[7] Istvan, M. S., Kurelek, J. W., & Yarusevych, S. (2018). Turbulence intensity effects on laminar separation bubbles formed over an airfoil. *AIAA Journal*, *56*(4), 1335-1347.
[8] Roberts, S. K., & Yaras, M. I. (2006). Effects of surface-roughness geometry on separation-bubble transition. *Journal of Turbomachinery*, *128*, 349-356.

[9] Menter, F. R., Langtry, R. B., Likki, S. R., Suzen, Y. B., Huang, P. G., & Völker, S. (2006). A correlation-based transition model using local variables—part I: model formulation. *Journal of Turbomachinery*, *128*(3), 413-422.
[10] Menter, F. R., Langtry, R., & Völker, S. (2006). Transition modelling for general purpose CFD codes. *Flow, turbulence and combustion*, *77*(1-4), 277-303.
[11] Rezaeiha, A., Montazeri, H., & Blocken, B. (2019). On the accuracy of turbulence models for CFD simulations of vertical axis wind turbines. *Energy*, *180*, 838-857.
[12] Marsh, P., Ranmuthugala, D., Penesis, I., & Thomas, G. (2017). The influence of turbulence model and two and three-dimensional domain selection on the simulated performance characteristics of vertical axis tidal turbines. *Renewable Energy*, *105*, 106-116.
[13] Rezaeiha, A., Montazeri, H., & Blocken, B. (2018). Towards accurate CFD simulations of vertical axis wind turbines at different tip speed ratios and solidities: Guidelines for azimuthal increment, domain size and convergence. *Energy conversion and management*, *156*, 301-316.
[14] Lam, H. F., & Peng, H. Y. (2016). Study of wake characteristics of a vertical axis wind turbine by two-and three-dimensional computational fluid dynamics simulations. *Renewable Energy*, *90*, 386-398.
[15] Rezaeiha, A., Kalkman, I., & Blocken, B. (2017). Effect of pitch angle on power performance and aerodynamics of a vertical axis wind turbine. *Applied energy*, *197*, 132-150.
[16] Rezaeiha, A., Kalkman, I., Montazeri, H., & Blocken, B. (2017). Effect of the shaft on the aerodynamic performance of urban vertical axis wind turbines. *Energy conversion and management*, *149*, 616-630.
[17] Zhu, H., Hao, W., Li, C., & Ding, Q. (2019). Numerical study of effect of solidity on vertical axis wind turbine with Gurney flap. *Journal of Wind Engineering and Industrial Aerodynamics*, *186*, 17-31.
[18] Lind, A. H., Jarugumilli, T., Benedict, M., Lakshminarayan, V. K., Jones, A. R., & Chopra, I. (2014). Flow field studies on a micro-air-vehicle-scale cycloidal rotor in forward flight. *Experiments in fluids*, *55*(12), 1-17.
[19] Paillard, B., Astolfi, J. A., & Hauville, F. (2015). URANSE simulation of an active variable-pitch cross-flow Darrieus tidal turbine: Sinusoidal pitch function investigation. *International Journal of Marine Energy*, *11*, 9-26.
[20] Chen, B., Su, S., Viola, I. M., & Greated, C. A. (2018). Numerical investigation of vertical-axis tidal turbines with sinusoidal pitching blades. *Ocean Engineering*, *155*, 75-87.

[21] Chen, B., Nagata, S., Murakami, T., & Ning, D. (2019). Improvement of sinusoidal pitch for vertical-axis hydrokinetic turbines and influence of rotational inertia. *Ocean Engineering*, *179*, 273-284.
[22] Benedict, M., Jarugumilli, T., Lakshminarayan, V., & Chopra, I. (2014). Effect of flow curvature on forward flight performance of a micro-air-vehicle-scale cycloidal-rotor. *AIAA Journal*, *52*(6), 1159-1169.
[23] Benedict, M., Jarugumilli, T., & Chopra, I. (2013). Effect of rotor geometry and blade kinematics on cycloidal rotor hover performance. *Journal of Aircraft*, *50*(5), 1340-1352.
[24] Benedict, M., Jarugumilli, T., & Chopra, I. (2016). Effects of asymmetric blade-pitching kinematics on forward-flight performance of a micro-air-vehicle-scale cycloidal-rotor. *Journal of Aircraft*, *53*(5), 1568-1573.
[25] Walther, C. M., Saemi, F., Benedict, M., & Lakshminarayan, V. (2019). Symmetric versus asymmetric pitching of a cycloidal rotor blade at ultra-low Reynolds numbers. *Journal of Aircraft*, *56*(3), 1179-1199.
[26] Menter, F. R., Kuntz, M., & Langtry, R. (2003). Ten years of industrial experience with the SST turbulence model. *Turbulence, Heat and Mass Transfer*, *4*(1), 625-632.
[27] Roesler, B. T., Kawamura, M. L., Miller, E., Wilson, M., Brink-Roby, J., Clemmenson, E., Keller, M., & Epps, B. P. (2016). Experimental performance of a novel trochoidal propeller. *Journal of Ship Research*, *60*(1), 48-60.
[28] Jarugumilli, T. (2013). An experimental investigation of a micro air vehicle-scale cycloidal rotor in forward flight. Master of science, URI: http://hdl.handle.net/1903/14822.
[29] Langtry, R. B., Menter, F. R., Likki, S. R., Suzen, Y. B., Huang, P. G., & Vo¨ lker, S. (2004). A correlation-based transition model using local variables: Part II—test cases and industrial applications. *ASME-GT2004-53454, ASME TURBO EXPO 2004, Vienna, Austria*.
[30] Gauthier, E., Kinsey, T., & Dumas, G. (2016). Impact of blockage on the hydrodynamic performance of oscillating-foils hydrokinetic turbines. *Journal of Fluids Engineering*, 138(9), 091103 (1-13).
[31] Kinsey, T., & Dumas, G. (2012). Computational fluid dynamics analysis of a hydrokinetic turbine based on oscillating hydrofoils. *Journal of Fluids Engineering*, *134*(2), 021104 (1-16).
[32] Winslow, J., Otsuka, H., Govindarajan, B., & Chopra, I. (2018). Basic understanding of airfoil characteristics at low Reynolds numbers (10^4–10^5). *Journal of Aircraft*, *55*(3), 1050-1061.

[33] Dong, H., Xia, T., Chen, L., Liu, S., Cui, Y. D., Khoo, B. C., & Zhao, A. (2019). Study on flow separation and transition of the airfoil in low Reynolds number. *Physics of Fluids*, *31*(10), 103601 (1-9).
[34] Negi, P. S., Vinuesa, R., Hanifi, A., Schlatter, P., & Henningson, D. S. (2018). Unsteady aerodynamic effects in small-amplitude pitch oscillations of an airfoil. *International Journal of Heat and Fluid Flow*, *71*, 378-391.
[35] Pascazio, M., Autric, J., Favier, D., & Maresca, C. (1996). Unsteady boundary-layer measurement on oscillating airfoils-Transition and separation phenomena in pitching motion. In *34th Aerospace Sciences Meeting and Exhibit* (p.35).